

Energy dependent chemical potentials of light hadrons and quarks based on transverse momentum spectra and yield ratios of negative to positive particles

Xing-Wei He^a, Feng-Min Wu^{a,b}, Hua-Rong Wei^{c,1}, and Bi-Hai Hong^c

^a*Institute of Theoretical Physics & State Key Laboratory of Quantum Optics and Quantum Optics Devices, Shanxi University, Taiyuan, Shanxi 030006, People's Republic of China*

^b*Department of Physics, Zhejiang Sci-Tech University, Hangzhou, Zhejiang 310000, People's Republic of China*

^c*Institute of Optoelectronic Technology, Lishui University, Lishui, Zhejiang 323000, People's Republic of China*

Abstract: We describe the transverse momentum spectra or transverse mass spectra of π^\pm , K^\pm , p , and \bar{p} produced in central gold-gold (Au-Au), central lead-lead (Pb-Pb), and inelastic proton-proton (pp) collisions at different collision energies range from the AGS to LHC by using a two-component (in most cases) Erlang distribution in the framework of multi-source thermal model. The fitting results are consistent with the experimental data, and the final-state yield ratios of negative to positive particles are obtained based on the normalization constants from the above describing the transverse momentum (or mass) spectra. The energy dependent chemical potentials of light hadrons (π , K , and p) and quarks (u , d , and s) in central Au-Au, central Pb-Pb, and inelastic pp collisions, are then extracted from the modified yield ratios in which the contributions of strong decay from high-mass resonance and weak decay from heavy flavor hadrons are removed. The study shows that most types of energy dependent chemical potentials decrease with increase of collision energy over a range from the AGS to LHC. The curves of all types of energy dependent chemical potentials, obtained from the fits of yield ratios vs energy, have the maximum at about 3.510 GeV, which possibly is the critical energy of phase transition from a liquid-like hadron state to a gas-like quark state in the collision system. At the top RHIC and LHC, all types of chemical potentials become small and tend to zero at very high energy, which confirms that the high energy collision system possibly changes completely from the liquid-like hadron-dominant state to the gas-like quark-dominant state and the partonic interactions possibly play a dominant role at the LHC.

Keywords: transverse momentum spectra, yield ratios of negative to positive particles, chemical potentials of particles, critical end point of phase transition

PACS: 14.65.Bt, 13.85.Hd, 24.10.Pa

1 Introduction

The critical energy of phase transition [1–4] is important for studying the quantum chromodynamics (QCD) phase diagram [5, 6] and the properties of quark-gluon plasma (QGP) [7–9], so more and more scientists devote to finding the critical energy. The experiments performed on the Relativistic Heavy Ion Collider (RHIC) and the Large Hadron Collider (LHC), especially the beam energy scan program at the RHIC, deal with a collision energy range from a few to several tens of GeV [1, 7, 10, 11], which may contain the energy of the critical end point of hadron-quark phase transition [1–4, 12]. The STAR Collaboration found that the critical energy may be or below 19.6 GeV (unless otherwise noted, the energy values presented in this paper are in the center-of-mass coordinate system) [1]. One study based

¹E-mail: huarongwei@qq.com; huarongwei@lsu.edu.cn

on yield ratio (the yield ratio of negative to positive particles) and the correlation between collision energy and transverse momentum indicated that the critical energy maybe range from 11.5 GeV to 19.6 GeV [1, 13–15], while another study based on yield ratio showed that the critical energy may be about 4 GeV [12]. Studies about a striking pattern of viscous damping and an excitation function for $(R_{out}^2 - R_{side}^2)$ extracted for central collisions indicated the critical energy may be close to 62.4 GeV [16–18]. It is not hard to see that the value of critical energy has not been determined so far, so finding the critical energy arouses our great interest.

Lattice QCD [19–21], a powerful tool to investigate the QGP matter in high-temperature and high-density system, indicates that the critical end point (CEP) of phase transition on QCD phase diagram is a crossover at small chemical potentials or high collision energies [22, 23]. So it is important to study baryon chemical potential for finding the CEP on QCD phase diagram. When collisions occur at high energy, especially at RHIC and LHC, the collision system probably creates the QGP matter [24–26] where the partonic interactions play an important role, and the baryon chemical potential is small, even close to 1 MeV or zero [12, 27–29]. While when energy is not very high, the transition from hadron to quark has not yet taken place in the collision system, where the hadronic interactions play an important role [1, 13–15], and the value of baryon chemical potential is larger. We could predict that the chemical potential corresponding to the CEP should be a inflection point or abrupt change point in chemical potential-energy plane. It is therefore worthwhile to study the trend of chemical potential with energy.

The yield ratio of negative to positive particles is an important quantity in high energy study. Generally, one can get yield ratio by many ways. One way is to directly collect the values of yield ratio from the productive international collaborations, which is a rapid and convenient method. Another way needs the aid of the extracted normalization constant in describing the transverse momentum spectra of negative and positive particles with consistent statistical law, but the workload is huge. In this paper, due to the fact that experiment data of some particles correspond to a narrow range of transverse momentum (p_T), we adopt the second method to obtain a relatively accurate result for the normalization constant being extracted from a wider range of transverse momentum distribution. In addition, one can extract the yield ratio as a fitting parameter in many models. One can obtain some information about the very hot and dense nuclear matter by yield ratio. For example, one can analyze some statistical thermal models to extract temperature, baryon chemical potential (μ_B) at chemical freez-out and so on by describing the ratios of hadron yields, and further to establish the "line of chemical freez-out" [30] by which one can continue to study QGP, QCD phase transition, and QCD phase diagram [7, 31–35]. Except for baryon chemical potential, one can study the chemical potentials of other hadrons and quarks because these chemical potentials are also important in studying collision system evolution and particle production.

In the present work, we describe the transverse momentum (p_T) or transverse mass (m_T) spectra of π^\pm , K^\pm , p , and \bar{p} produced in central gold-gold (Au-Au), central lead-lead (Pb-Pb) and inelastic proton-proton (pp) collisions in mid-rapidity interval (in most cases) over a center-of-mass energy ($\sqrt{s_{NN}}$) range from the AGS to LHC [36–51] by using a two-component (in most cases) Erlang distribution [52, 53] in the framework of a multi-source thermal model [53–55], and obtain the yield ratios, π^-/π^+ , K^-/K^+ , and \bar{p}/p , of negative to positive particles according to the extracted normalization constants. The energy dependent chemical potentials of light hadrons (π , K , and p) and quarks (u , d , and s) in central Au-Au, central Pb-Pb, and inelastic pp collisions are then extracted from the modified yield ratios in which the contributions of strong decay from high-mass resonance and weak decay from heavy flavor hadrons are removed.

2 The model and formulism

According to our method, to obtain the normalization constants, we need firstly to describe the p_T spectra of π^\pm , K^\pm , p , and \bar{p} with a multi-component Erlang distribution [52, 53] which is in the framework of a multi-source thermal model [53–55]. The model assumes that many emission sources are formed in

high energy collisions and are classified into a few groups due to the existent of different interacting mechanisms in the collisions and different event samples in experiment measurements. The sources in the same group have the same excitation degree and stay at a common local equilibrium state, which can be described by a Erlang p_T distribution. All emission sources in different groups result in the final-state distribution, which can be described by a multi-component Erlang p_T distribution.

The multi-component Erlang distribution based on the above multi-source thermal model has the following form. According to thermodynamic system, particles generated from one emission source obey to an exponential distribution of transverse momentum,

$$f_{ij}(p_{tij}) = \frac{1}{\langle p_{tij} \rangle} \exp \left[- \frac{p_{tij}}{\langle p_{tij} \rangle} \right], \quad (1)$$

where p_{tij} is the transverse momentum of the i -th source in the j -th group, and $\langle p_{tij} \rangle$ is the mean value of p_{tij} . We assume that the source number in the j -th group and the transverse momentum of the m_j sources are denoted by m_j and p_T , respectively. All the sources in the j -th group then result in the folding result of exponential distribution

$$f_j(p_T) = \frac{p_T^{m_j-1}}{(m_j-1)! \langle p_{tij} \rangle^{m_j}} \exp \left[- \frac{p_T}{\langle p_{tij} \rangle} \right], \quad (2)$$

which is the normalized Erlang distribution. The contribution of the l group of sources can be expressed as

$$f(p_T) = \sum_{j=1}^l k_j f_j(p_T), \quad (3)$$

where k_j denotes the relative weight contributed by the j th group and meets the normalization $\sum_{j=1}^l k_j = 1$. This is the multi-component Erlang distribution.

In fact, in the present work, we describe the transverse momentum spectra of final-state light flavour particles by using a two-component Erlang distribution, where one component reflects the soft excitation process, while the other one reflects the hard scattering process. The soft process corresponding to low- p_T region is regarded as the contribution of the interactions among a few sea quarks and gluons, and the hard process corresponding to high- p_T region is regarded as originating from a harder head-on scattering between a few valent quarks. Due to the fact that the experimental data of some particles correspond to a narrow range of p_T , we adopt one-component Erlang distribution to fit these data.

Some experimental data we collect are about transverse mass distribution, not p_T distribution, so we give the transformational relation between p_T distribution and m_T distribution based on the relation between p_T and m_T ($m_T = \sqrt{p_T^2 + m_0^2}$, where m_0 is the rest mass of particle), i.e.

$$\frac{dN}{N dm_T} = \frac{m_T}{p_T} \frac{dN}{N dp_T}. \quad (4)$$

The same as in our previous work [28], in the present work, we only calculate the chemical potentials of some light hadrons (π , K , and p), and some light quarks (u , d , and s). For the hadrons containing c or b quark, considering that there is a lack of the experimental data of p_T spectra continuously varying with energy, we do not calculate the chemical potentials of the hadrons containing c or b quark, and c and b quarks. In addition, due to the lifetimes of the hadrons containing t quark being too short to measure, we also can not obtain the chemical potentials of the hadrons containing t quark. According to the statistical arguments based on the chemical and thermal equilibrium within the thermal and statistical model [56], we can get the relations between antiparticle to particle (negative to positive particle) yield ratios and

chemical potentials of hadrons to be [42, 56, 57]

$$\begin{aligned} k_\pi &= \exp\left(-\frac{2\mu_\pi}{T_{ch}}\right), \\ k_K &= \exp\left(-\frac{2\mu_K}{T_{ch}}\right), \\ k_p &= \exp\left(-\frac{2\mu_p}{T_{ch}}\right), \end{aligned} \quad (5)$$

where k_π , k_K , and k_p denote the yield ratios of antiparticles, π^- , K^- , and \bar{p} , to particles, π^+ , K^+ , and p , respectively, and μ_π , μ_K , and μ_p represent the chemical potentials of π , K , and p , respectively. In addition, T_{ch} represents the chemical freeze-out temperature of interacting system, and can be empirically obtained by the following formula

$$T_{ch} = T_{\text{lim}} \frac{1}{1 + \exp[2.60 - \ln(\sqrt{s_{NN}})/0.45]} \quad (6)$$

within the framework of a statistical thermal model of non-interacting gas particles with the assumption of standard Maxwell-Boltzmann statistics [7, 8, 58], where the ‘limiting’ temperature T_{lim} is 0.164 GeV, and $\sqrt{s_{NN}}$ is in the unit of GeV [58, 59].

Assuming that μ_u , μ_d , and μ_s represent the chemical potentials of u , d , and s quarks, respectively, and according to Equation (5) and references [12, 57, 60] under the same value of chemical freeze-out temperature, the yield ratios in terms of quark chemical potentials can be written as

$$\begin{aligned} k_\pi &= \exp\left[-\frac{(\mu_u - \mu_d)}{T_{ch}}\right] / \exp\left[\frac{(\mu_u - \mu_d)}{T_{ch}}\right] = \exp\left[-\frac{2(\mu_u - \mu_d)}{T_{ch}}\right], \\ k_K &= \exp\left[-\frac{(\mu_u - \mu_s)}{T_{ch}}\right] / \exp\left[\frac{(\mu_u - \mu_s)}{T_{ch}}\right] = \exp\left[-\frac{2(\mu_u - \mu_s)}{T_{ch}}\right], \\ k_p &= \exp\left[-\frac{(2\mu_u + \mu_d)}{T_{ch}}\right] / \exp\left[\frac{(2\mu_u + \mu_d)}{T_{ch}}\right] = \exp\left[-\frac{2(2\mu_u + \mu_d)}{T_{ch}}\right]. \end{aligned} \quad (7)$$

Based on Equations (5) and (7), one can obtain the chemical potentials of hadrons and quarks in terms of yield ratios respectively,

$$\begin{aligned} \mu_\pi &= -\frac{1}{2}T_{ch} \cdot \ln(k_\pi), \\ \mu_K &= -\frac{1}{2}T_{ch} \cdot \ln(k_K), \\ \mu_p &= -\frac{1}{2}T_{ch} \cdot \ln(k_p), \end{aligned} \quad (8)$$

and

$$\begin{aligned} \mu_u &= -\frac{1}{6}T_{ch} \cdot \ln(k_\pi \cdot k_p), \\ \mu_d &= -\frac{1}{6}T_{ch} \cdot \ln(k_\pi^{-2} \cdot k_p), \\ \mu_s &= -\frac{1}{6}T_{ch} \cdot \ln(k_\pi \cdot k_K^{-3} \cdot k_p). \end{aligned} \quad (9)$$

In the present work, by describing the p_T (or m_T) spectra of some light particles, π^\pm , K^\pm , p , and \bar{p} in central Au-Au, central Pb-Pb, and inelastic pp collisions in mid-rapidity interval at collision energy from the AGS to LHC with a two-component (in most cases) Erlang distribution, we obtain the yield ratios, π^-/π^+ , K^-/K^+ , and \bar{p}/p based on the extracted normalization constants, and the chemical potentials of light hadrons (π , K , and p) and light quarks (u , d , and s) based on the yield ratios modified by removing

the contributions of strong decay from high-mass resonance and weak decay from heavy flavor hadrons. Then the dependencies of chemical potentials on $\sqrt{s_{NN}}$ are analyzed.

3 Results and discussion

Figure 1 shows the transverse mass distributions of π^\pm [Figures 1(a) and 1(b)] and K^\pm [Figures 1(c) and 1(d)] produced in central (0–5%) Au-Au collisions at mid-rapidity in the center-of-mass energy ($\sqrt{s_{NN}}$) range from 2.67 to 4.84 GeV, where dN/dy on axis denote the rapidity density. The experimental data represented by different kinds of symbols were measured by the E895 Collaboration [36] for π^\pm at 2.67, 3.31, 3.81, and 4.28 GeV, and the E866 and E917 Collaborations [37, 38] for K^\pm at 3.31, 3.81, 4.28 and 4.84 GeV. The data at each energy are scaled by suitable factors for clarity. The plotted errors bars include both statistical and systematic uncertainties for π^\pm and only statistical uncertainty for K^\pm . The solid curves are our results calculated by using the two-component Erlang distribution. The values of free parameters (m_1 , p_{ti1} , k_1 , m_2 , and p_{ti2}), normalization constant (N_0), and χ^2 per degree of freedom (χ^2/dof), and p-values corresponding to the two-component Erlang distribution are listed in Table 1, where the normalization constant is for comparison between curve and data. Here, χ^2 is calculated according to the following formula of

$$\chi^2 = \sum \frac{(N_i^{exp} - N_i^{theo})^2}{\sigma^2} \quad (10)$$

where N_i^{exp} , N_i^{theo} and σ denote experimental value, theoretical value, and error value, respectively. One can see that the two-component Erlang distribution can well describe the experimental data of the considered particles in Au-Au collisions at the AGS. The values of m_2 corresponding to high- p_T region for different particles are 2, which reflects that the hard process origins from a hard head-on scattering between two valent quarks, while the values of m_1 corresponding to low- p_T region for different particles are 3, which reflects that the soft process origins from the interaction among a few sea quarks and gluons. The values of weight factor k_1 of soft excitation process are more than 50%, which shows that soft excitation is the main excitation process, and the normalization constants N_0 increases with increase of energy. It should be noted that the particle yield ratio is represented by N_0 from the spectrum of negative or positive particles. The relative value of N_0 is enough to obtain the particle yield ratio.

Figure 2 presents the transverse momentum spectra of π^\pm , K^\pm , p , and \bar{p} in central (0–5%) Au-Au collisions at center-of-mass energy 7.7 [Figures 2(a) and 2(d)], 11.5 (Figures 2(b) and 2(e)), and 19.6 [Figures 2(c) and 2(f)] GeV. The symbols represent the experimental data recorded by the STAR Collaboration in the mid-rapidity range $|y| < 0.1$ [39]. The uncertainties are statistical and systematic added in quadrature. The curves are our results fitted by using the two-component Erlang distribution. The values of m_1 , p_{ti1} , k_1 , m_2 , p_{ti2} , N_0 , and χ^2/dof , and p-values corresponding to the two-component Erlang distribution are given in Table 1. It is not hard to see that the experimental data can be well fitted by the two-component Erlang distribution. Similarly, the values of m_2 are 2, and the values of m_1 are 2, 3, and 4. The values of weight factor k_1 are more than 50%, and N_0 in most cases increases with increase of collision energy.

Figure 3 gives the same as Figure 2 but for Au-Au collisions at 27 [Figures 3(a) and 3(d)], 39 [Figures 3(b) and 3(e)], and 62.4 [Figures 3(c) and 3(f)] GeV. All the experimental data were recorded by the STAR Collaboration [39, 40]. The results calculated by using the two-component Erlang distribution are shown in the solid curves, where the values of corresponding free parameters, normalization constant, and χ^2/dof , and p-values are shown in Table 2. Obviously, the calculation results by the two-component Erlang distribution are in good agreement with the experimental data of the considered particles in Au-Au collisions. Once more, the values of m_2 are 2, and the values of m_1 are 2, 3, and 4. The values of weight factor k_1 are more than 50%, and N_0 in most cases increases with increase of collision energy.

The p_T spectra of π^\pm , K^\pm , p , and \bar{p} in central (0–5%) Au-Au collisions at 130 [Figures 4(a) and 4(c)], 200 [Figures 4(b) and 4(d)] GeV are displayed in Figure 4. The symbols also denote the experimental

data recorded by the PHENIX Collaboration [41, 42]. The data for each type of particle are divided by suitable factors for clarity. The error bars indicate the combined uncorrelated statistical and systematic uncertainties for 130 GeV, and are statistical only for 200 GeV. The curves are the two-component Erlang model fits to the spectra. The values of all free parameters, normalization constant, and χ^2/dof , and p-values corresponding to the two-component Erlang distribution are listed in Table 2. Similarly, our calculation results with the two-component Erlang model are consistent with the experimental data. The values of m_2 are 2, and the values of m_1 are 2, 3, and 4. The values of weight factor k_1 are more than 50%, and N_0 in most cases increases with increase of collision energy.

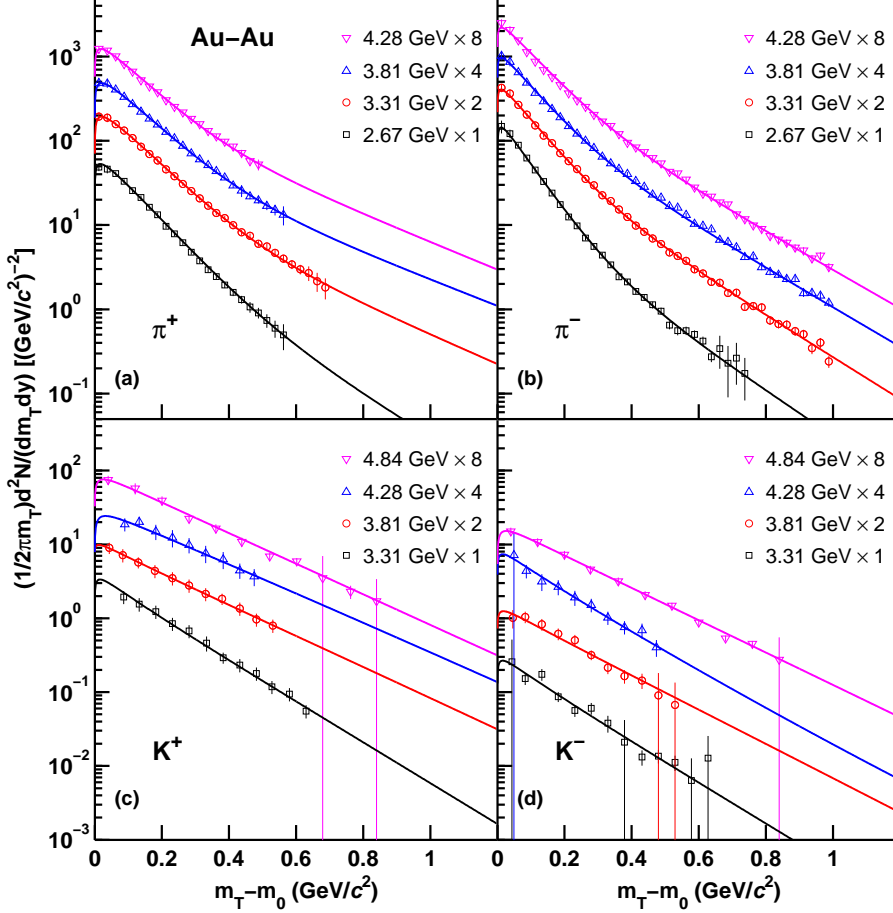


Figure 1. Transverse mass spectra for positive (π^+ , K^+) and negative (π^- , K^-) particles produced in central Au-Au collisions at mid-rapidity over a energy range from 2.67 to 4.84 GeV. The experimental data represented by the symbols are measured by the E895 Collaboration [36] for π^\pm at 2.67, 3.31, 3.81, and 4.28 GeV, and the E866 and E917 Collaborations [37, 38] for K^\pm at 3.31, 3.81, 4.28 and 4.84 GeV. The data at each energy are scaled by successive powers of 2 for clarity. The plotted errors bars include both statistical and systematic uncertainties for π^\pm and only statistical uncertainty for K^\pm . The solid curves are our results calculated by using the two-component Erlang distribution.

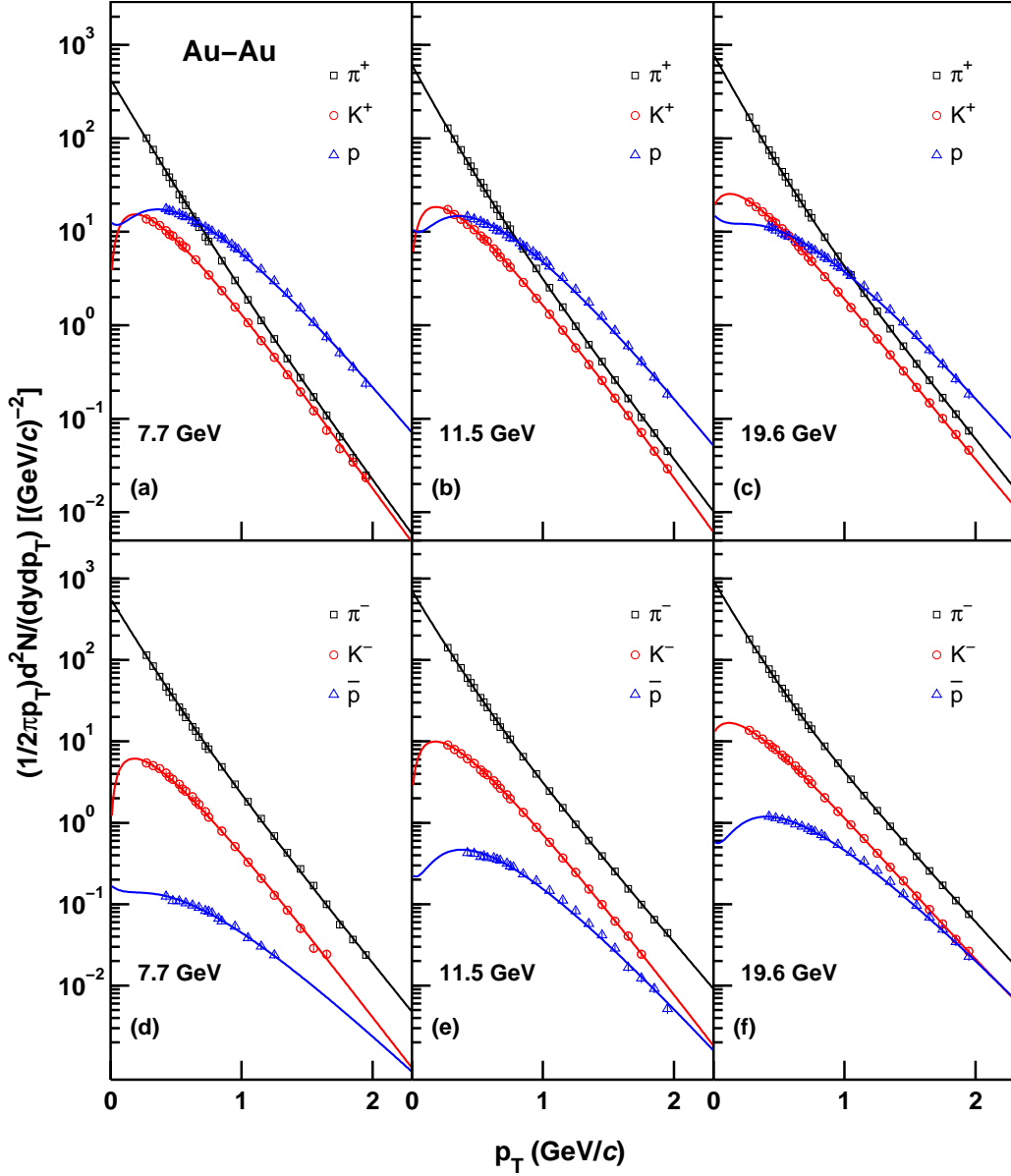


Figure 2. Mid-rapidity transverse momentum spectra for positive (π^+ , K^+ , p) and negative (π^- , K^- , \bar{p}) particles produced in central Au-Au collisions at 7.7 [Figures 2(a) and 2(d)], 11.5 [Figures 2(b) and 2(e)], and 19.6 [Figures 2(c) and 2(f)] GeV. The symbols represent the experimental data recorded by the STAR Collaboration [39]. The errors are the combined statistical and systematic ones, and the curves are our results by the two-component Erlang distribution.

Table 1. Values of free parameters, normalization constant, and χ^2/dof , and p-values corresponding to two-component Erlang p_T (or m_T) distribution for Au-Au collisions in Figures 1 and 2.

Figure	$\sqrt{s_{NN}}$ (GeV)	Particle	m_1	$\langle p_{ti1} \rangle$ (GeV/c)	k_1	m_2	$\langle p_{ti2} \rangle$ (GeV/c)	N_0	χ^2/dof	p-value
Figure 1 (a)	2.67	π^+	3	0.078 ± 0.001	0.74 ± 0.01	2	0.182 ± 0.012	12.051 ± 0.365	7.043/17	0.983
Figure 1 (b)		π^-	3	0.061 ± 0.001	0.74 ± 0.02	2	0.163 ± 0.010	20.811 ± 0.365	11.690/24	0.983
Figure 1 (a)	3.31	π^+	3	0.083 ± 0.002	0.68 ± 0.02	2	0.251 ± 0.010	27.819 ± 0.747	3.768/22	1
Figure 1 (c)		K^+	3	0.149 ± 0.003	0.91 ± 0.06	2	0.162 ± 0.020	2.344 ± 0.172	2.144/6	0.906
Figure 1 (b)		π^-	3	0.067 ± 0.001	0.58 ± 0.01	2	0.176 ± 0.004	38.257 ± 0.777	19.052/34	0.982
Figure 1 (d)		K^-	3	0.149 ± 0.008	0.91 ± 0.06	2	0.162 ± 0.060	0.186 ± 0.017	8.857/7	0.263
Figure 1 (a)	3.81	π^+	3	0.084 ± 0.002	0.60 ± 0.02	2	0.280 ± 0.010	39.084 ± 0.770	2.654/17	1
Figure 1 (c)		K^+	3	0.190 ± 0.011	0.80 ± 0.06	2	0.202 ± 0.023	4.829 ± 0.285	0.431/5	0.994
Figure 1 (b)		π^-	3	0.068 ± 0.001	0.51 ± 0.01	2	0.187 ± 0.004	50.197 ± 0.797	36.777/34	0.341
Figure 1 (d)		K^-	3	0.174 ± 0.007	0.88 ± 0.06	2	0.185 ± 0.026	0.572 ± 0.007	3.598/5	0.608
Figure 1 (a)	4.28	π^+	3	0.081 ± 0.003	0.51 ± 0.02	2	0.267 ± 0.016	49.619 ± 1.103	5.465/14	0.978
Figure 1 (c)		K^+	3	0.197 ± 0.011	0.94 ± 0.04	2	0.235 ± 0.030	7.717 ± 0.031	1.304/3	0.728
Figure 1 (b)		π^-	3	0.072 ± 0.003	0.51 ± 0.02	2	0.192 ± 0.002	62.627 ± 0.744	40.248/34	0.213
Figure 1 (d)		K^-	3	0.150 ± 0.009	0.80 ± 0.07	2	0.235 ± 0.032	1.355 ± 0.107	1.738/4	0.784
Figure 1 (c)	4.84	K^+	3	0.187 ± 0.006	0.87 ± 0.07	2	0.267 ± 0.040	10.798 ± 0.383	5.328/5	0.377
Figure 1 (d)		K^-	3	0.180 ± 0.003	0.91 ± 0.06	2	0.247 ± 0.030	2.025 ± 0.069	5.463/5	0.362
Figure 2 (a)	7.7	π^+	2	0.172 ± 0.004	0.63 ± 0.06	2	0.233 ± 0.004	96.122 ± 3.326	13.970/20	0.832
		K^+	3	0.197 ± 0.003	0.93 ± 0.07	2	0.300 ± 0.033	20.070 ± 0.662	6.218/17	0.991
		p	4	0.215 ± 0.003	0.89 ± 0.08	2	0.270 ± 0.054	52.211 ± 2.203	5.070/23	1
Figure 2 (d)		π^-	2	0.149 ± 0.006	0.52 ± 0.03	2	0.219 ± 0.003	107.122 ± 3.578	9.297/20	0.979
		K^-	3	0.186 ± 0.003	0.92 ± 0.08	2	0.285 ± 0.057	7.208 ± 0.268	14.213/17	0.652
		\bar{p}	4	0.232 ± 0.013	0.71 ± 0.14	2	0.334 ± 0.066	0.412 ± 0.020	2.045/9	0.991
Figure 2 (b)	11.5	π^+	2	0.153 ± 0.007	0.52 ± 0.04	2	0.236 ± 0.003	125.208 ± 4.583	2.186/20	1
		K^+	3	0.201 ± 0.003	0.87 ± 0.13	2	0.262 ± 0.048	24.436 ± 0.718	1.486/19	1
		p	4	0.211 ± 0.003	0.90 ± 0.08	2	0.244 ± 0.048	42.924 ± 1.871	7.386/22	0.998
Figure 2 (e)		π^-	2	0.146 ± 0.008	0.51 ± 0.04	2	0.230 ± 0.003	135.170 ± 5.785	1.593/20	1
		K^-	3	0.191 ± 0.003	0.92 ± 0.08	2	0.221 ± 0.044	12.017 ± 0.382	1.338/17	1
		\bar{p}	4	0.209 ± 0.004	0.92 ± 0.08	2	0.234 ± 0.046	1.374 ± 0.059	17.977/17	0.390
Figure 2 (c)	19.6	π^+	2	0.156 ± 0.008	0.57 ± 0.05	2	0.249 ± 0.005	165.077 ± 7.957	0.737/20	1
		K^+	3	0.198 ± 0.005	0.67 ± 0.13	2	0.294 ± 0.009	29.706 ± 0.879	1.316/20	1
		p	4	0.224 ± 0.004	0.79 ± 0.07	2	0.278 ± 0.040	34.690 ± 1.374	4.885/23	1
Figure 2 (f)		π^-	2	0.145 ± 0.008	0.56 ± 0.04	2	0.246 ± 0.004	176.077 ± 8.381	0.682/20	1
		K^-	3	0.192 ± 0.004	0.64 ± 0.07	2	0.292 ± 0.007	18.620 ± 0.585	2.950/20	1
		\bar{p}	4	0.222 ± 0.004	0.93 ± 0.07	2	0.247 ± 0.049	3.937 ± 0.169	7.144/16	0.970

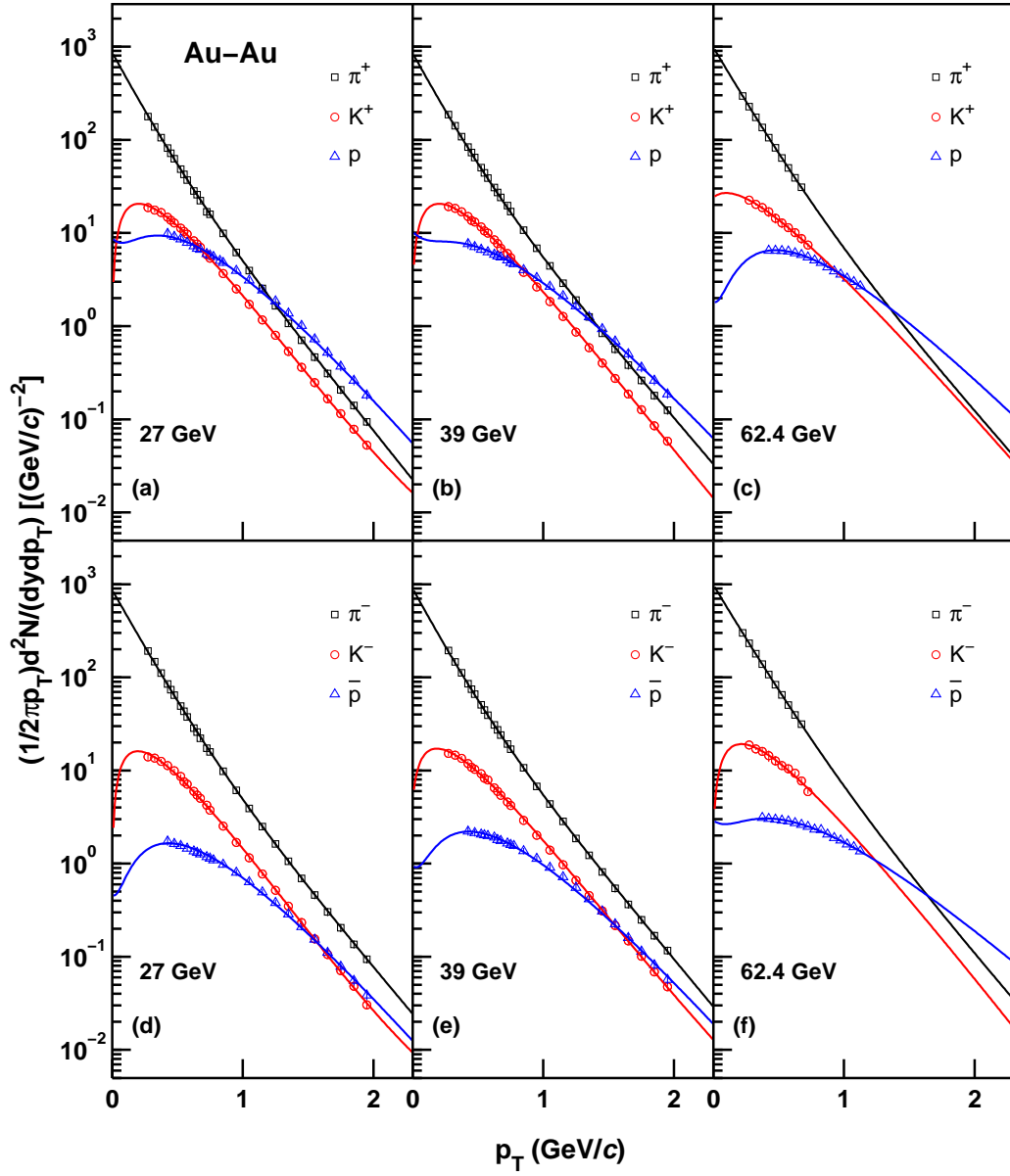


Figure 3. Same as Figure 2 but for Au-Au collisions at 27 [Figures 3(a) and 3(d)], 39 [Figures 3(b) and 3(e)], and 62.4 [Figures 3(c) and 3(f)] GeV.

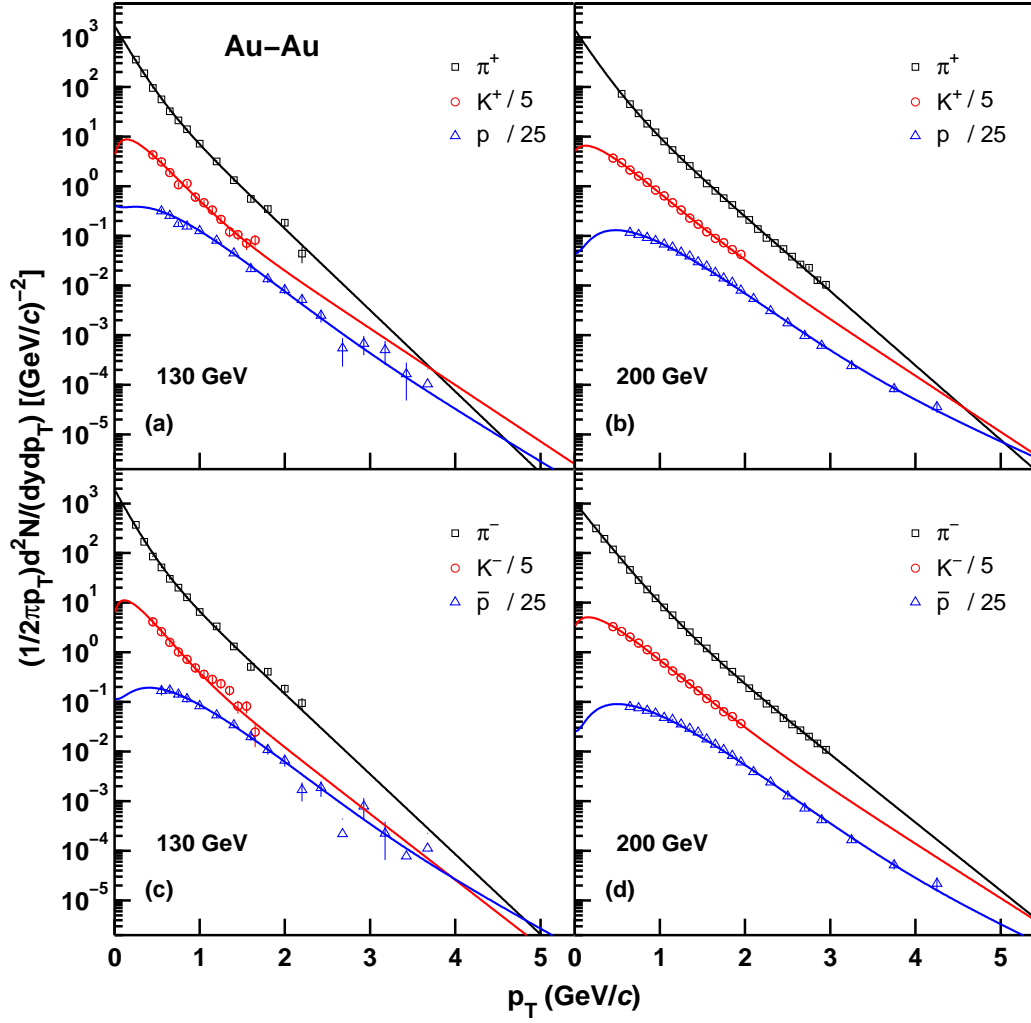


Figure 4. Same as Figure 2 but for Au-Au collisions at 130 [Figures 4(a) and 4(c)], 200 (Figures 4(b) and 4(d)] GeV.

Table 2. Values of free parameters, normalization constant, and χ^2/dof , and p-values corresponding to two-component Erlang p_T (or m_T) distribution for Au-Au collisions in Figures 3 and 4.

Figure	$\sqrt{s_{NN}}$ (GeV)	Particle	m_1	$\langle p_{ti1} \rangle$ (GeV/c)	k_1	m_2	$\langle p_{ti2} \rangle$ (GeV/c)	N_0	χ^2/dof	p-value
Figure 3 (a)	27	π^+	2	0.152 ± 0.007	0.51 ± 0.05	2	0.249 ± 0.003	182.402 ± 6.202	2.449/20	1
		K^+	3	0.205 ± 0.004	0.97 ± 0.02	2	0.575 ± 0.115	29.993 ± 1.046	2.393/20	1
		p	4	0.226 ± 0.005	0.85 ± 0.12	2	0.284 ± 0.056	30.191 ± 1.165	4.566/17	0.999
Figure 3 (d)		π^-	2	0.164 ± 0.006	0.66 ± 0.04	2	0.264 ± 0.004	186.402 ± 6.710	2.325/20	1
		K^-	3	0.198 ± 0.002	0.97 ± 0.01	2	0.531 ± 0.052	21.872 ± 0.819	8.210/19	0.984
		\bar{p}	4	0.228 ± 0.004	0.92 ± 0.08	2	0.343 ± 0.068	5.877 ± 0.239	5.235/16	0.994
Figure 3 (b)	39	π^+	2	0.155 ± 0.008	0.54 ± 0.05	2	0.265 ± 0.004	185.159 ± 7.258	3.265/20	1
		K^+	3	0.211 ± 0.003	0.94 ± 0.06	2	0.359 ± 0.045	31.219 ± 1.024	5.650/20	0.999
		p	4	0.239 ± 0.005	0.79 ± 0.09	2	0.293 ± 0.055	26.115 ± 1.081	3.078/16	1
Figure 3 (e)		π^-	2	0.153 ± 0.010	0.53 ± 0.04	2	0.258 ± 0.004	191.409 ± 7.159	1.088/20	1
		K^-	3	0.206 ± 0.003	0.86 ± 0.06	2	0.352 ± 0.020	24.658 ± 0.715	5.446/20	0.999
		\bar{p}	4	0.233 ± 0.004	0.92 ± 0.08	2	0.280 ± 0.056	8.086 ± 0.319	5.566/17	0.996
Figure 3 (c)	62.4	π^+	2	0.172 ± 0.003	0.65 ± 0.05	2	0.274 ± 0.012	232.461 ± 1.720	0.261/4	0.992
		K^+	3	0.246 ± 0.004	0.75 ± 0.04	2	0.256 ± 0.015	39.598 ± 2.032	0.463/4	0.977
		p	4	0.252 ± 0.001	0.92 ± 0.03	2	0.436 ± 0.027	28.457 ± 0.154	2.891/9	0.968
Figure 3 (f)		π^-	2	0.175 ± 0.002	0.67 ± 0.05	2	0.269 ± 0.008	234.954 ± 1.269	0.825/4	0.935
		K^-	3	0.223 ± 0.015	0.90 ± 0.10	2	0.239 ± 0.047	32.071 ± 1.844	6.873/4	0.143
		\bar{p}	4	0.281 ± 0.002	0.77 ± 0.03	2	0.435 ± 0.010	15.011 ± 0.117	11.697/10	0.306
Figure 4 (a)	130	π^+	2	0.128 ± 0.003	0.58 ± 0.02	2	0.262 ± 0.020	288.154 ± 9.350	19.320/8	0.013
		K^+	3	0.166 ± 0.007	0.65 ± 0.03	2	0.382 ± 0.030	46.172 ± 1.883	11.031/7	0.137
		p	4	0.224 ± 0.008	0.61 ± 0.04	2	0.420 ± 0.015	29.451 ± 0.552	12.703/11	0.313
Figure 4 (c)		π^-	2	0.115 ± 0.010	0.60 ± 0.02	2	0.269 ± 0.012	291.470 ± 9.100	25.039/8	0.002
		K^-	3	0.143 ± 0.007	0.59 ± 0.04	2	0.326 ± 0.016	44.407 ± 1.933	11.880/7	0.104
		\bar{p}	4	0.240 ± 0.007	0.79 ± 0.04	2	0.466 ± 0.030	18.813 ± 0.644	17.215/11	0.102
Figure 4 (b)	200	π^+	2	0.162 ± 0.008	0.62 ± 0.02	2	0.291 ± 0.004	314.469 ± 3.500	37.817/19	0.006
		K^+	3	0.208 ± 0.003	0.60 ± 0.03	2	0.409 ± 0.006	47.468 ± 0.793	28.553/10	0.002
		p	4	0.266 ± 0.003	0.92 ± 0.02	2	0.568 ± 0.007	15.345 ± 0.266	19.924/16	0.224
Figure 4 (d)		π^-	2	0.179 ± 0.004	0.65 ± 0.01	2	0.297 ± 0.001	293.451 ± 2.500	38.653/22	0.016
		K^-	3	0.223 ± 0.002	0.79 ± 0.01	2	0.480 ± 0.007	42.471 ± 0.456	9.724/10	0.465
		\bar{p}	4	0.270 ± 0.003	0.98 ± 0.02	2	0.650 ± 0.006	11.195 ± 0.225	26.068/16	0.053

Figure 5 exhibits the m_T spectra of π^\pm at $0 < y < 0.2$, K^\pm at $|y| < 0.1$, p , and \bar{p} produced in central Pb-Pb collisions at 6.3 [Figures 5(a) and 5(d)], 7.7 [Figures 5(b) and 5(e)], and 8.8 [Figures 5(c) and 5(f)] GeV. The experimental data, represented by symbols, were taken by the NA49 Collaboration [43–45], where p and \bar{p} were done near mid-rapidity and covered the rapidity intervals of $1.5 < y < 2.2$ ($y_{c.m.} = 1.88$) for 6.3 GeV, $1.6 < y < 2.3$ ($y_{c.m.} = 2.08$) for 7.7 GeV, and $1.9 < y < 2.3$ ($y_{c.m.} = 2.22$) for 8.8 GeV. The error bars on the spectra points are statistical only. The curves are fits of two-component Erlang function to the spectra. The values of free parameters, normalization constant, and χ^2/dof , and p-values are summarized in Table 3. We can see that the experimental data for all hadrons and energies are well described by the fit function. The values of m_2 are 2, and the values of m_1 are 2, 3, and 4. The values of weight factor k_1 are more than 50%, and N_0 increases with increase of collision energy.

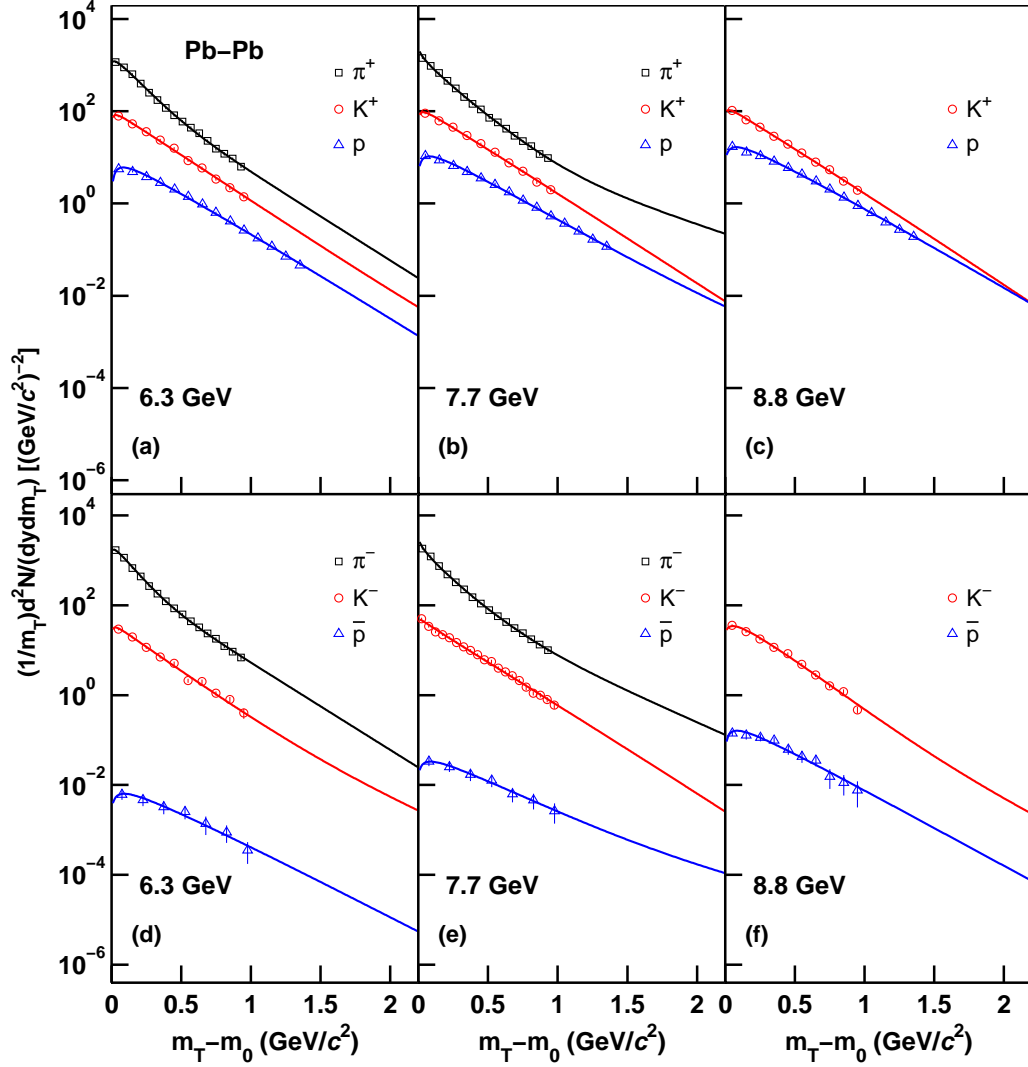


Figure 5. Transverse mass spectra for π^\pm , K^\pm , p , and \bar{p} in central Pb-Pb collisions at 6.3 [Figures 5(a) and 5(d)], 7.7 [Figures 5(b) and 5(e)], and 8.8 [Figures 5(c) and 5(f)] GeV. The symbols represent the experimental data taken by the NA49 Collaboration [43–45]. The errors are statistical only. The curves are fits of two-component Erlang function to the spectra.

Figure 6 presents the m_T and p_T spectra of π^\pm , K^\pm , p , and \bar{p} in central Pb-Pb collisions at 12.3 ([Figures 6(a) and 6(d)], 17.3 [Figures 6(b) and 6(e)], and 2760 [Figures 6(c) and 6(f)] GeV, where

σ_{trig} on the vertical axis denotes the interaction cross section satisfying a T0 centrality trigger. The symbols represent the experimental data reported by the NA49 Collaboration for 12.3 GeV at mid-rapidity ($|y| < 0.1$ for K^\pm [45], $2.2 < y < 2.6$ ($y_{c.m.} = 2.57$) for p and \bar{p} [44]), the NA44 Collaboration for 17.3 GeV near mid-rapidity ($2.4 < y < 3.1$ for π^\pm , $2.4 < y < 3.5$ for K^\pm , and $2.3 < y < 2.9$ for p and \bar{p}) [46], and the ALICE Collaboration for 2760 GeV at mid-rapidity $|y| < 0.5$ [47]. Some data for different particles are divided by suitable factors for clarity. The errors are statistical for 12.3 GeV, are systematic for 17.3 GeV, and are quadratic sum of statistical errors and systematic errors for 2760 GeV. The curves represent the two-component Erlang fits. The values of free parameters, normalization constant, and χ^2/dof , and p-values are summarized in Table 3. Obviously, the experimental data for all particles at all energies are in good agreement with the fits. The values of m_2 are 2, and the values of m_1 are 2, 3, and 4. The values of weight factor k_1 are more than 50%, and N_0 increases with increase of collision energy.

Figure 7 shows the p_T spectra of π^\pm [Figures 7(a) and 7(b)] and K^\pm [Figures 7(c) and 7(d)] produced in mid-rapidity $y \approx 0$ inelastic pp collisions at 6.3, 7.7, 8.8, 12.3, and 17.3 GeV. The measurements were performed at the CERN-Super Proton Synchrotron (SPS) by the large acceptance NA61/SHINE hadron spectrometer [48]. Spectra at different energies are scaled by appropriate factors for better visibility. The error bars on data points correspond to combined statistical and systematic uncertainties. The curves are our fitting results by using the one- or two-component Erlang function. For some curves, we use one-component Erlang function because the number of corresponding experimental data points is small. Due to the proportion of the second component is small, it has little effect on the calculated particle ratio, despite the absence of the second component. The values of free parameters, normalization constant, and χ^2/dof , and p-values are given in Table 4. As can be seen, the fits for all hadrons at all energies are in good agreement with the experimental data. The values of m_2 and m_1 are 2 and 3, respectively. The values of weight factor k_1 are more than 50%. It should be noted that the dof for π^- at 12.3 GeV in Table 4 is zero, which means the dash curve in Figure 7(b) is drawn to guide the eye.

Figure 8 presents the p_T spectra of π^\pm , K^\pm , p , and \bar{p} produced in inelastic pp collisions at 62.4 [Figures 8(a) and 8(c)] and 200 [Figures 8(b) and 8(d)] GeV, where E and σ on the vertical axis denote the particle energy and cross-section, respectively. The data measured by the PHENIX Collaboration in the mid-pseudorapidity range $|\eta| < 0.35$ [49], are represented in different panels by different symbols. Spectra for different particles are scaled by appropriate factors for better visibility. The error bars are statistical only. The curves are our results fitted by using the two-component Erlang distribution. The values of free parameters, normalization constant, and χ^2/dof , and p-values are given in Table 4. One can see that all the fitting results by using the two-component Erlang function are consistent with the experimental data. The values of m_2 are 2, and the values of m_1 are 2, 3, and 4. The values of weight factor k_1 are more than 50%, and N_0 increases with increase of collision energy.

Figure 9 exhibits the p_T spectra of π^\pm , K^\pm , p , and \bar{p} produced in inelastic pp collisions at 900 GeV [Figures 9(a) and 9(c)] and 2.76 TeV [Figures 9(b) and 9(d)]. The symbols also denote the experimental data recorded by the CMS Collaboration in the range $|y| < 1$ [50]. The data for different particles are scaled by suitable factors for clarity. The error bars indicate the combined uncorrelated statistical and systematic uncertainties, and the fully correlated normalization uncertainty is 3.0%. The curves are fits of the two-component Erlang function to the spectra. The values of free parameters, normalization constant, and χ^2/dof , and p-values are summarized in Table 5. We can see that the experimental data are well described by the fit function. The values of m_2 are 2, and the values of m_1 are 2, 3, and 4. The values of weight factor k_1 are more than 50%, and N_0 increases with increase of collision energy.

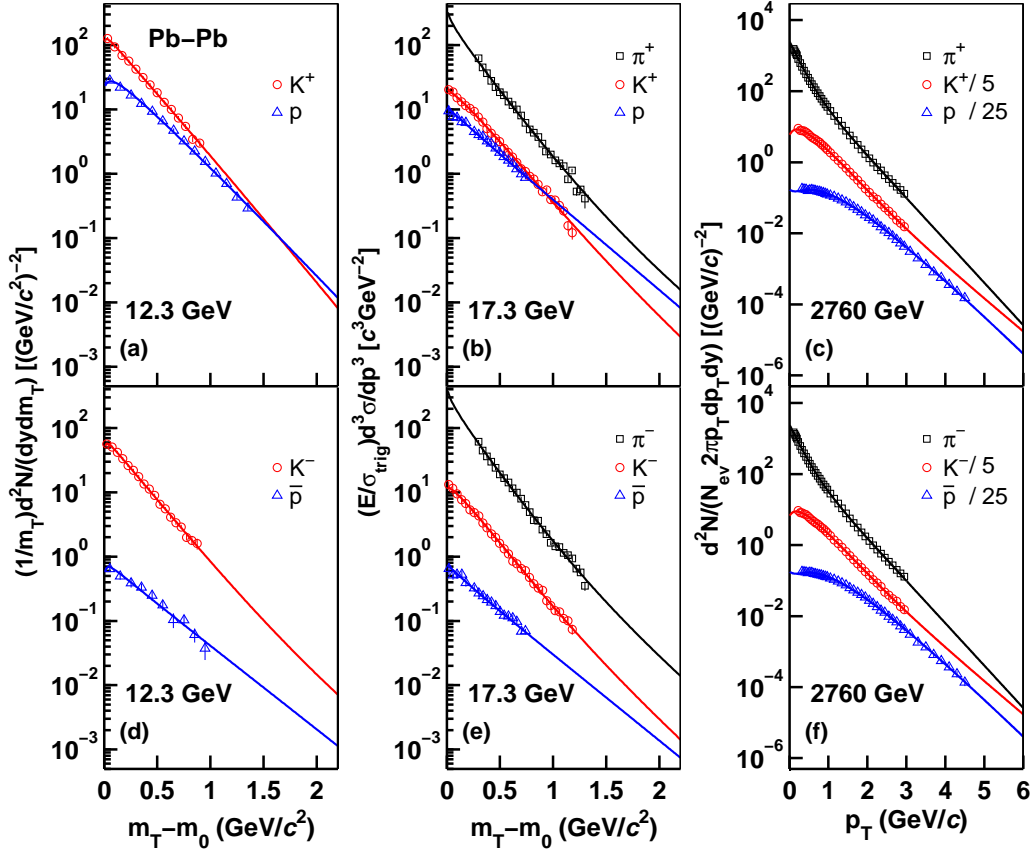


Figure 6. Transverse mass and momentum spectra for π^\pm , K^\pm , p , and \bar{p} at mid-rapidity in central Pb-Pb collisions at 12.3 [Figures 6(a) and 6(d)], 17.3 [Figures 6(b) and 6(e)], and 2760 [Figures 6(c) and 6(f)] GeV. The symbols represent the experimental data reported by the NA49 Collaboration for 12.3 GeV at mid-rapidity ($|y| < 0.1$ for K^\pm [45], $2.2 < y < 2.6$ ($y_{c.m.} = 2.57$) for p and \bar{p} [44]), the NA44 Collaboration for 17.3 GeV near mid-rapidity ($2.4 < y < 3.1$ for π^\pm , $2.4 < y < 3.5$ for K^\pm , and $2.3 < y < 2.9$ for p and \bar{p}) [46], and the ALICE Collaboration for 2760 GeV at mid-rapidity $|y| < 0.5$ [47]. Some data for different particles are divided by suitable factors for clarity. The errors are statistical for 12.3 GeV, are systematic for 17.3 GeV, and are quadratic sum of statistical errors and systematic errors for 2760 GeV. The curves are fits of two-component Erlang function to the spectra.

Table 3. Values of free parameters, normalization constant, and χ^2/dof , and p-values corresponding to two-component Erlang p_T (or m_T) distribution for Pb-Pb collisions in Figures 5 and 6.

Figure	$\sqrt{s_{NN}}$ (GeV)	Particle	m_1	$\langle p_{ti1} \rangle$ (GeV/c)	k_1	m_2	$\langle p_{ti2} \rangle$ (GeV/c)	N_0	χ^2/dof	p-value
Figure 5 (a)	6.3	π^+	3	0.095 ± 0.003	0.51 ± 0.03	2	0.228 ± 0.005	72.088 ± 2.379	9.764/10	0.461
		K^+	3	0.194 ± 0.004	0.90 ± 0.10	2	0.295 ± 0.059	16.508 ± 0.644	6.875/4	0.143
		p	4	0.209 ± 0.002	1	-	-	2.889 ± 0.078	27.988/11	0.003
Figure 5 (d)		π^-	3	0.082 ± 0.003	0.51 ± 0.03	2	0.225 ± 0.006	83.773 ± 2.765	4.884/10	0.899
		K^-	3	0.179 ± 0.005	0.86 ± 0.09	2	0.328 ± 0.081	5.644 ± 0.186	13.617/4	0.009
		\bar{p}	4	0.234 ± 0.018	1	-	-	0.004 ± 0.001	1.420/4	0.841
Figure 5 (b)	7.7	π^+	2	0.172 ± 0.003	0.90 ± 0.02	2	0.436 ± 0.079	87.611 ± 2.541	10.081/10	0.433
		K^+	3	0.202 ± 0.004	1	-	-	20.584 ± 0.638	6.746/4	0.456
		p	4	0.214 ± 0.004	0.87 ± 0.12	2	0.420 ± 0.055	5.278 ± 0.306	2.421/8	0.965
Figure 5 (e)		π^-	2	0.151 ± 0.004	0.79 ± 0.03	2	0.317 ± 0.022	98.711 ± 3.257	4.493/10	0.922
		K^-	3	0.205 ± 0.006	0.82 ± 0.08	2	0.220 ± 0.038	8.170 ± 0.302	18.012/14	0.206
		\bar{p}	4	0.233 ± 0.028	0.75 ± 0.15	2	0.580 ± 0.116	0.021 ± 0.004	0.4253/1	0.514
Figure 5 (c)	8.8	K^+	3	0.203 ± 0.004	0.91 ± 0.05	2	0.205 ± 0.041	21.556 ± 0.625	5.397/4	0.249
		p	4	0.221 ± 0.003	0.92 ± 0.08	2	0.270 ± 0.054	8.605 ± 0.422	7.546/8	0.479
Figure 5 (f)		K^-	4	0.149 ± 0.004	0.75 ± 0.15	2	0.280 ± 0.031	8.062 ± 0.282	13.337/4	0.010
		\bar{p}	4	0.219 ± 0.010	0.92 ± 0.07	2	0.370 ± 0.074	0.084 ± 0.010	3.408/4	0.492
Figure 6 (a)	12.3	K^+	3	0.204 ± 0.004	0.90 ± 0.07	2	0.220 ± 0.027	24.872 ± 0.696	6.261/8	0.618
		p	4	0.224 ± 0.003	0.85 ± 0.07	2	0.290 ± 0.046	13.871 ± 0.569	8.960/8	0.346
Figure 6 (d)		K^-	3	0.192 ± 0.004	0.83 ± 0.07	2	0.327 ± 0.065	11.307 ± 0.339	5.198/12	0.951
		\bar{p}	3	0.312 ± 0.010	0.94 ± 0.06	2	0.370 ± 0.074	0.348 ± 0.022	3.947/4	0.413
Figure 6 (b)	17.3	π^+	2	0.199 ± 0.004	0.91 ± 0.04	2	0.330 ± 0.038	17.753 ± 0.781	44.048/20	0.001
		K^+	4	0.162 ± 0.005	0.51 ± 0.06	2	0.289 ± 0.014	4.246 ± 0.238	19.806/24	0.708
		p	3	0.292 ± 0.008	0.96 ± 0.02	2	0.322 ± 0.020	0.403 ± 0.014	6.545/12	0.886
Figure 6 (e)		π^-	2	0.188 ± 0.003	0.88 ± 0.03	2	0.307 ± 0.014	18.926 ± 0.662	24.600/20	0.217
		K^-	4	0.150 ± 0.005	0.51 ± 0.10	2	0.286 ± 0.011	2.378 ± 0.131	9.820/24	0.995
		\bar{p}	3	0.304 ± 0.011	0.93 ± 0.03	2	0.170 ± 0.034	0.028 ± 0.002	7.744/12	0.805
Figure 6 (c)	2760	π^+	2	0.177 ± 0.007	0.58 ± 0.03	2	0.364 ± 0.004	118.422 ± 3.790	14.385/35	0.999
		K^+	3	0.283 ± 0.009	0.64 ± 0.10	2	0.473 ± 0.021	17.258 ± 0.552	2.657/30	1
		p	4	0.360 ± 0.005	0.82 ± 0.05	2	0.470 ± 0.064	5.311 ± 0.175	9.093/36	1
Figure 6 (f)		π^-	2	0.180 ± 0.007	0.58 ± 0.03	2	0.364 ± 0.004	118.191 ± 3.782	12.640/35	0.999
		K^-	3	0.277 ± 0.010	0.59 ± 0.09	2	0.467 ± 0.016	17.198 ± 0.602	2.851/30	1
		\bar{p}	4	0.360 ± 0.006	0.81 ± 0.07	2	0.470 ± 0.076	5.253 ± 0.173	10.028/36	1

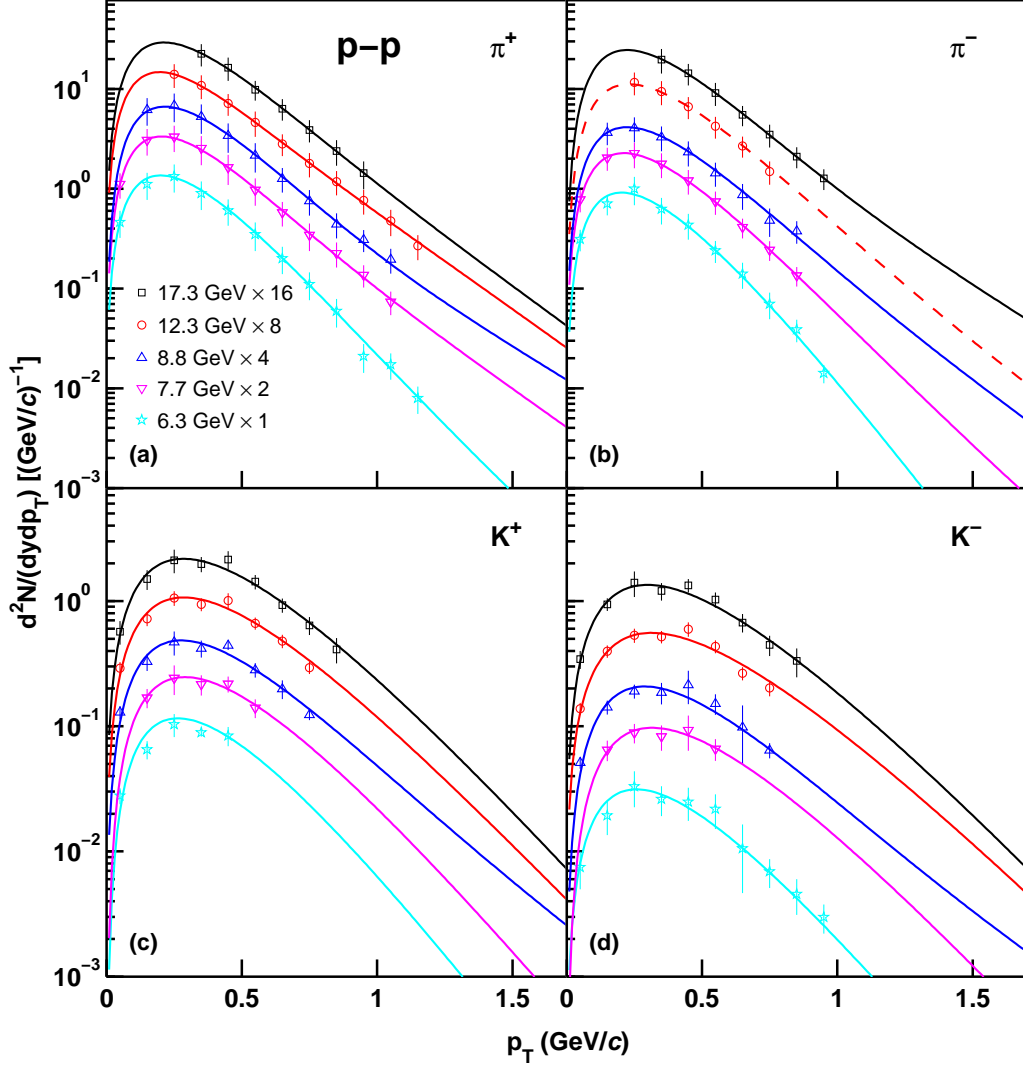


Figure 7. Transverse momentum spectra for π^\pm [Figures 7(a) and 7(b)] and K^\pm [Figures 7(c) and 7(d)] in $y \approx 0$ inelastic pp collisions at SPS energies (6.3, 7.7, 8.8, 12.3, and 17.3 GeV). The symbols represent the experimental data reported by the NA61/SHINE Collaboration [48]. Spectra at different energies are scaled by appropriate factors for better visibility. The errors are quadratic sum of statistical errors and systematic errors. The curves are fits of one- or two-component Erlang function to the spectra, where the dash curve in the figure is drawn to guide the eye.

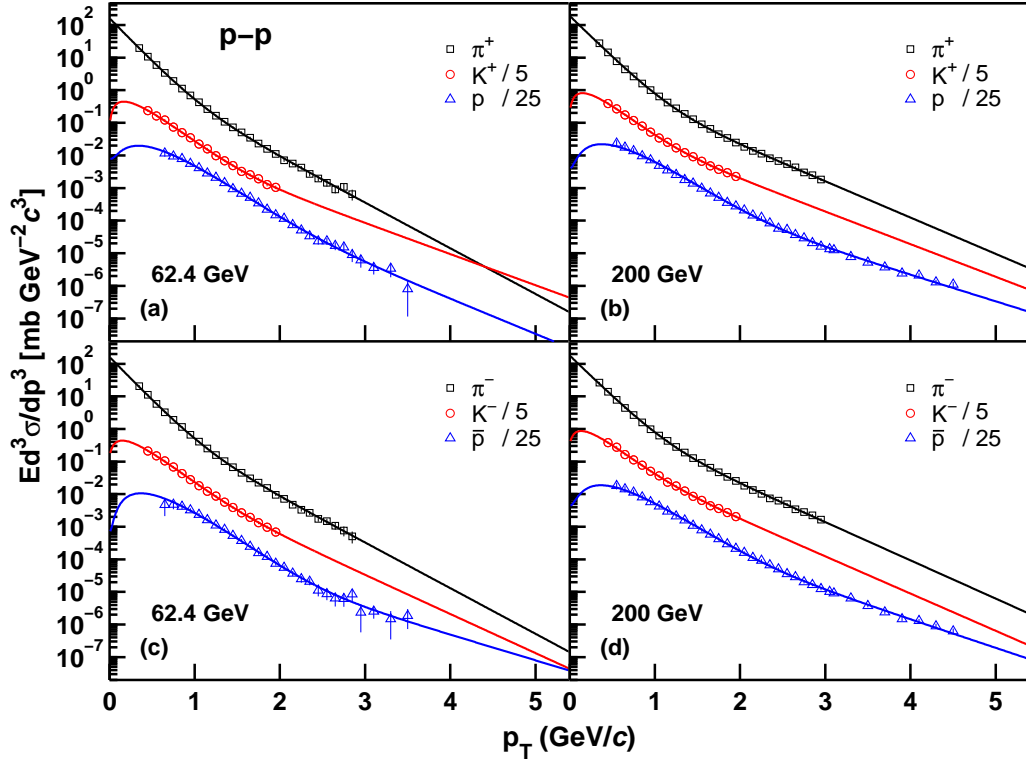


Figure 8. Transverse momentum spectra for positive (π^+ , K^+ , p) and negative (π^- , K^- , \bar{p}) particles produced in inelastic pp collisions at 62.4 [Figures 8(a) and 8(c)] and 200 [Figures 8(b) and 8(d)] GeV. The experimental data represented by the symbols are measured by the PHENIX Collaboration in $|\eta| < 0.35$ [49]. The errors, are statistical only. The curves are fits by the two-component Erlang distribution.

Table 4. Values of free parameters, normalization constant, and χ^2/dof , and p-values corresponding to one- or two-component Erlang p_T distribution for inelastic pp collisions in Figures 7 and 8.

Figure	$\sqrt{s_{NN}}$ (GeV)	Particle	m_1	$\langle p_{t1} \rangle$ (GeV/c)	k_1	m_2	$\langle p_{t2} \rangle$ (GeV/c)	N_0	χ^2/dof	p-value
Figure 7 (a)	6.3	π^+	3	0.103 ± 0.006	0.77 ± 0.09	2	0.163 ± 0.011	0.538 ± 0.051	2.193/6	0.901
Figure 7 (c)		K^+	3	0.143 ± 0.012	1	-	-	0.056 ± 0.001	12.005/2	0.002
Figure 7 (b)		π^-	3	0.106 ± 0.002	0.90 ± 0.06	2	0.116 ± 0.010	0.358 ± 0.038	1.874/4	0.759
Figure 7 (d)		K^-	3	0.135 ± 0.008	0.80 ± 0.07	2	0.184 ± 0.020	0.016 ± 0.003	2.566/4	0.632
Figure 7 (a)	7.7	π^+	3	0.102 ± 0.008	0.69 ± 0.08	2	0.202 ± 0.011	0.698 ± 0.086	0.246/5	0.998
Figure 7 (c)		K^+	3	0.145 ± 0.013	1	-	-	0.066 ± 0.006	0.862/2	0.650
Figure 7 (b)		π^-	3	0.110 ± 0.042	0.73 ± 0.12	2	0.170 ± 0.012	0.482 ± 0.078	0.084/3	0.993
Figure 7 (d)		K^-	3	0.158 ± 0.017	1	-	-	0.028 ± 0.001	0.487/2	0.784
Figure 7 (a)	8.8	π^+	3	0.107 ± 0.004	0.80 ± 0.04	2	0.232 ± 0.015	0.711 ± 0.055	0.370/4	0.985
Figure 7 (c)		K^+	3	0.144 ± 0.004	0.75 ± 0.07	2	0.190 ± 0.060	0.067 ± 0.001	5.585/2	0.061
Figure 7 (b)		π^-	3	0.113 ± 0.005	0.75 ± 0.06	2	0.203 ± 0.018	0.461 ± 0.038	0.653/2	0.722
Figure 7 (d)		K^-	3	0.162 ± 0.007	0.75 ± 0.08	2	0.193 ± 0.090	0.030 ± 0.001	1.179/2	0.411
Figure 7 (a)	12.3	π^+	3	0.098 ± 0.009	0.51 ± 0.04	2	0.198 ± 0.008	0.796 ± 0.068	0.212/4	0.995
Figure 7 (c)		K^+	3	0.155 ± 0.005	0.76 ± 0.07	2	0.180 ± 0.030	0.076 ± 0.003	4.164/2	0.125
Figure 7 (b)		π^-	3	0.117 ± 0.009	0.80 ± 0.09	2	0.202 ± 0.016	0.631 ± 0.089	0.165/0	0
Figure 7 (d)		K^-	3	0.159 ± 0.004	0.64 ± 0.06	2	0.246 ± 0.030	0.044 ± 0.001	4.512/2	0.105
Figure 7 (a)	17.3	π^+	3	0.108 ± 0.008	0.61 ± 0.08	2	0.198 ± 0.017	0.813 ± 0.049	0.054/1	0.817
Figure 7 (c)		K^+	3	0.154 ± 0.007	0.80 ± 0.06	2	0.178 ± 0.030	0.077 ± 0.006	2.300/3	0.512
Figure 7 (b)		π^-	3	0.112 ± 0.006	0.77 ± 0.06	2	0.227 ± 0.020	0.688 ± 0.004	0.032/1	0.859
Figure 7 (d)		K^-	3	0.164 ± 0.008	0.80 ± 0.07	2	0.178 ± 0.030	0.051 ± 0.003	3.057/3	0.382
Figure 8 (a)	62.4	π^+	2	0.160 ± 0.003	0.88 ± 0.01	2	0.310 ± 0.005	0.965 ± 0.039	5.886/26	1
Figure 8 (c)		K^+	3	0.175 ± 0.003	0.84 ± 0.02	2	0.455 ± 0.019	0.085 ± 0.003	3.026/16	1
		p	4	0.186 ± 0.004	0.83 ± 0.04	2	0.404 ± 0.016	0.040 ± 0.002	6.489/27	1
		π^-	2	0.160 ± 0.003	0.89 ± 0.01	2	0.310 ± 0.004	0.966 ± 0.035	8.208/26	1
		K^-	3	0.168 ± 0.004	0.76 ± 0.03	2	0.362 ± 0.014	0.076 ± 0.003	1.856/16	1
	\bar{p}	4	0.186 ± 0.003	0.95 ± 0.02	2	0.552 ± 0.046	0.022 ± 0.001	7.113/27	1	
Figure 8 (b)	200	π^+	2	0.170 ± 0.003	0.91 ± 0.01	2	0.390 ± 0.004	1.071 ± 0.041	11.062/27	0.997
Figure 8 (d)		K^+	3	0.162 ± 0.004	0.73 ± 0.02	2	0.434 ± 0.012	0.120 ± 0.005	1.123/16	1
		p	4	0.194 ± 0.004	0.88 ± 0.01	2	0.532 ± 0.008	0.043 ± 0.002	17.121/34	0.993
		π^-	2	0.170 ± 0.003	0.89 ± 0.01	2	0.370 ± 0.004	1.028 ± 0.040	8.247/27	1
	K^-	3	0.156 ± 0.005	0.64 ± 0.03	2	0.380 ± 0.009	0.119 ± 0.005	3.264/16	1	
	\bar{p}	4	0.192 ± 0.004	0.86 ± 0.02	2	0.497 ± 0.006	0.036 ± 0.002	10.592/34	1	

Figure 10 shows the same as Fig. 9, but for $\sqrt{s} = 7$ TeV [Figures 10(a) and 10(c)] and $\sqrt{s} = 13$ TeV [Figures 10(b) and 10(d)]. The symbols also denote the experimental data recorded by the CMS collaboration in the range $|y| < 1$ [50, 51]. The error bars indicate the combined uncorrelated statistical and systematic uncertainties, and the fully correlated normalization uncertainty is 3.0%. The curves are our results fitted by using the two-component Erlang distribution. The values of free parameters, normalization constant, and χ^2/dof , and p-values are summarized in Table 5. It is not hard to see that the experimental data can be well fitted by the two-component Erlang distribution. Similarly, The values of m_2 are 2, and the values of m_1 are 2 and 3. The values of weight factor k_1 are more than 50%, and N_0 increases with increase of collision energy.

According to the extracted normalization constants from the above comparisons, the three types of energy dependent yield ratios, π^-/π^+ , K^-/K^+ , and \bar{p}/p , of negative to positive particles from different collision systems, are obtained and are shown in Figure 11. The black, red, and blue circles denote respectively the calculated results from inelastic pp , central Au-Au, and central Pb-Pb collisions. For comparison, the black, red, and blue triangles correspondingly denote the experimental results [36–48, 50, 51, 61–68] from inelastic or NSD pp , central Au-Au, and central Pb-Pb collisions, respectively. One can see that our calculation results based on transverse momentum (or mass) spectra are consistent with the experimental data. That means the differences between our calculation results and experimental data are very small, which indicates that our calculation method is correct.

In fact, the yield ratios we calculate on the basis of transverse momentum (or mass) spectra, are at the stage of kinetic freeze-out and are affected by strong decay from high-mass resonance and weak decay from heavy flavor hadrons. In order to obtain the yield ratios at the stage of chemical freeze-out, one need remove the contributions of strong decay and weak decay from the above yield ratios. According to

reference [70], we remove the contributions of strong and weak decays and obtain the modified (primary) yield ratios, k_π , k_K , and k_p . The calculation result shows that strong decay affects mainly k_π and k_K , and weak decay affects mainly k_p . Strong decay can pull down k_π and lift k_K , and weak decay can lift k_p , although these two decays do not significantly affect the primary yield ratios as a whole.

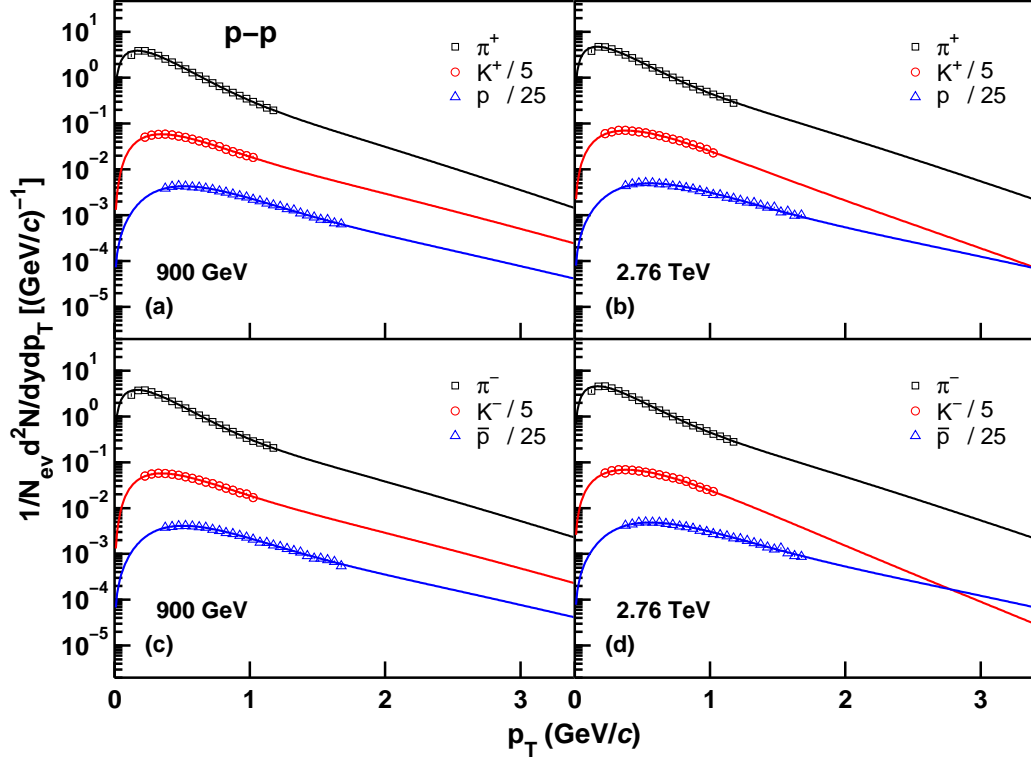


Figure 9. Transverse momentum spectra for positive (π^+ , K^+ , p) and negative (π^- , K^- , \bar{p}) particles produced in inelastic pp collisions at 900 GeV [Figures 9(a) and 9(c)] and 2.76 TeV [Figures 9(b) and 9(d)]. The symbols represent the experimental data recorded by the CMS Collaboration in $|y| < 1$ [50]. The errors are the combined uncorrelated statistical and systematic ones, and the fully correlated normalization uncertainty is 3.0%. The curves are our results fitted by the two-component Erlang distribution.

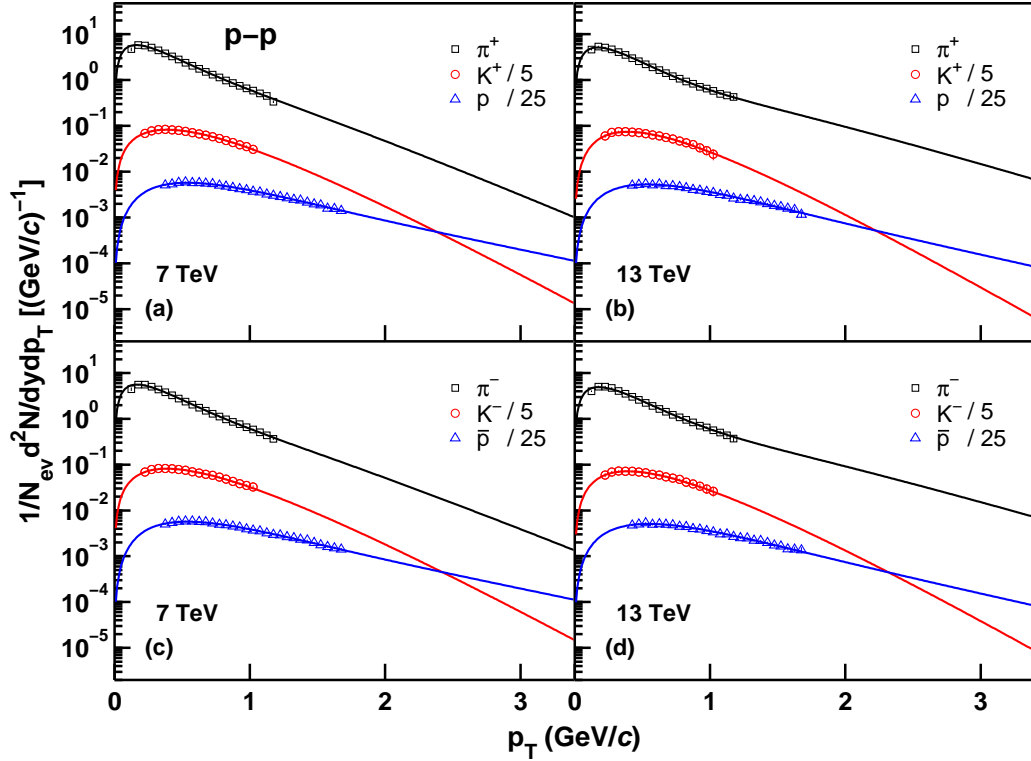


Figure 10. The same p_T spectra as Fig. 9, but for $\sqrt{s} = 7$ TeV [Figures 10(a) and 10(c)] and $\sqrt{s} = 13$ TeV [Figures 10(b) and 10(d)]. The symbols also represent the experimental data recorded by the CMS Collaboration in $|y| < 1$ [50, 51]. Similarly, the errors are the combined uncorrelated statistical and systematic ones, and the fully correlated normalization uncertainty is 3.0%. The curves are our results fitted by the two-component Erlang distribution.

Table 5. Values of free parameters, normalization constant, and χ^2/dof , and p-values corresponding to one- or two-component Erlang p_T distribution for inelastic pp collisions in Figures 9 and 10.

Figure	$\sqrt{s_{NN}}$ (GeV)	Particle	m_1	$\langle p_{ti1} \rangle$ (GeV/c)	k_1	m_2	$\langle p_{ti2} \rangle$ (GeV/c)	N_0	χ^2/dof	p-value
Figure 9 (a)	900	π^+	2	0.160 ± 0.002	0.80 ± 0.01	2	0.390 ± 0.017	3.924 ± 0.043	14.393/22	0.887
		K^+	3	0.165 ± 0.004	0.52 ± 0.03	2	0.465 ± 0.018	0.480 ± 0.006	1.769/17	1
		p	4	0.171 ± 0.003	0.51 ± 0.04	2	0.530 ± 0.020	0.212 ± 0.004	11.337/27	0.996
Figure 9 (c)		π^-	2	0.160 ± 0.002	0.80 ± 0.01	2	0.420 ± 0.018	3.884 ± 0.047	17.291/22	0.747
		K^-	3	0.165 ± 0.004	0.51 ± 0.03	2	0.460 ± 0.015	0.472 ± 0.006	2.163/17	1
		\bar{p}	4	0.168 ± 0.003	0.51 ± 0.02	2	0.536 ± 0.018	0.202 ± 0.003	19.958/27	0.833
Figure 9 (b)	2760	π^+	2	0.156 ± 0.002	0.73 ± 0.01	2	0.384 ± 0.011	4.944 ± 0.059	11.582/22	0.965
		K^+	3	0.190 ± 0.004	0.51 ± 0.04	2	0.370 ± 0.012	0.578 ± 0.008	6.135/17	0.992
		p	4	0.179 ± 0.004	0.51 ± 0.04	2	0.670 ± 0.027	0.276 ± 0.004	30.949/27	0.273
Figure 9 (d)		π^-	2	0.159 ± 0.002	0.74 ± 0.01	2	0.387 ± 0.011	4.824 ± 0.058	16.848/22	0.772
		K^-	3	0.201 ± 0.006	0.51 ± 0.07	2	0.330 ± 0.015	0.560 ± 0.008	9.175/17	0.935
		\bar{p}	4	0.181 ± 0.003	0.51 ± 0.03	2	0.610 ± 0.024	0.262 ± 0.004	32.664/27	0.208
Figure 10 (a)	7000	π^+	2	0.144 ± 0.002	0.60 ± 0.02	2	0.321 ± 0.007	6.084 ± 0.067	18.074/22	0.702
		K^+	3	0.236 ± 0.005	0.62 ± 0.05	2	0.260 ± 0.012	0.700 ± 0.009	3.234/17	1
		p	3	0.261 ± 0.006	0.51 ± 0.05	2	0.600 ± 0.025	0.346 ± 0.005	12.963/27	0.989
Figure 10 (c)		π^-	2	0.150 ± 0.002	0.63 ± 0.02	2	0.336 ± 0.007	5.984 ± 0.072	19.714/22	0.600
		K^-	3	0.240 ± 0.005	0.63 ± 0.06	2	0.251 ± 0.014	0.696 ± 0.008	6.961/17	0.984
		\bar{p}	3	0.260 ± 0.005	0.51 ± 0.05	2	0.600 ± 0.030	0.342 ± 0.005	19.058/27	0.868
Figure 10 (b)	13000	π^+	2	0.159 ± 0.004	0.70 ± 0.02	2	0.441 ± 0.027	5.724 ± 0.092	8.045/22	0.997
		K^+	3	0.219 ± 0.008	0.71 ± 0.12	2	0.266 ± 0.031	0.600 ± 0.013	3.199/17	1
		p	3	0.264 ± 0.009	0.51 ± 0.06	2	0.569 ± 0.037	0.314 ± 0.006	11.583/26	0.993
Figure 10 (d)		π^-	2	0.168 ± 0.002	0.73 ± 0.03	2	0.456 ± 0.039	5.604 ± 0.078	28.200/22	0.169
		K^-	3	0.230 ± 0.010	0.69 ± 0.10	2	0.250 ± 0.026	0.596 ± 0.015	2.820/17	1
		\bar{p}	3	0.270 ± 0.008	0.51 ± 0.06	2	0.569 ± 0.028	0.306 ± 0.006	10.087/26	0.998

The three types of yield ratios show regular trends with increase of collision energy. k_π from pp collisions, k_K , and k_p increase with increase of collision energy, and k_π from central Au-Au and central Pb-Pb collisions, decreases with increase of collision energy. To see more clearly the dependences of the three types of yield ratios on collision energy, we show the logarithms of the three yield ratios, $\ln(k_\pi)$, $\ln(k_K)$, and $\ln(k_p)$, with $1/\sqrt{s_{NN}}$ in Figure 12. The black squares, red circles, and blue triangles denote the calculated results from inelastic pp , central Au-Au, and central Pb-Pb collisions at mid-rapidity, respectively. One can see that $\ln(k_K)$ and $\ln(k_p)$ show obviously linear dependence on $1/\sqrt{s_{NN}}$, which should be fitted by linear functions for clarity. $\ln(k_K)$ and $\ln(k_p)$ from all collision systems mentioned above, decrease monotonously with increase of $1/\sqrt{s_{NN}}$, and can be described by the below linear functions of

$$\ln(k_K) = (-8.690 \pm 0.187)/\sqrt{s_{NN}} + (-0.021 \pm 0.030), \quad (11)$$

and

$$\ln(k_p) = (-45.034 \pm 0.637)/\sqrt{s_{NN}} + (-0.035 \pm 0.030), \quad (12)$$

with χ^2/dof to be 7.589/26 and 3.675/17 respectively. $\ln(k_\pi)$ displays different behavior from the above two yield ratios. With the increase of $\sqrt{s_{NN}}$, $\ln(k_\pi)$ from inelastic pp collisions increases obviously and that from nucleus-nucleus (Au-Au and Pb-Pb) collisions slightly decreases. The dependence of $\ln(k_\pi)$ on $1/\sqrt{s_{NN}}$ can also be empirically described by the following functions of

$$\ln(k_{\pi_{pp}}) = (-2.859 \pm 0.814)/\sqrt{s_{NN}} + (-0.016 \pm 0.045), \quad (13)$$

and

$$\ln(k_{\pi_{NN}}) = (2.890 \pm 1.084)/(\sqrt{s_{NN}})^2 + (0.205 \pm 0.142)/\sqrt{s_{NN}} + (-0.010 \pm 0.016), \quad (14)$$

with χ^2/dof to be 0.543/8 and 56.886/13 respectively, where $k_{\pi_{pp}}$ and $k_{\pi_{NN}}$ represent the k_π from pp and nucleus-nucleus (Au-Au and Pb-Pb) collisions, respectively. In fact, we also can use a linear function to

fit the energy dependent $k_{\pi_{NN}}$ roughly, but in order to more accurately describe the data points in low energy region, we adopt the above polynomial function. The fitting results are represented by the solid and dotted curves, where the solid curves correspond to the data points in the energy range mentioned above, and the dotted curves show the changed trends of data points. It is noticed that the values of intercepts of the above four curves are asymptotically 0, which means the limiting values of the three yield ratios are one at very high energy.

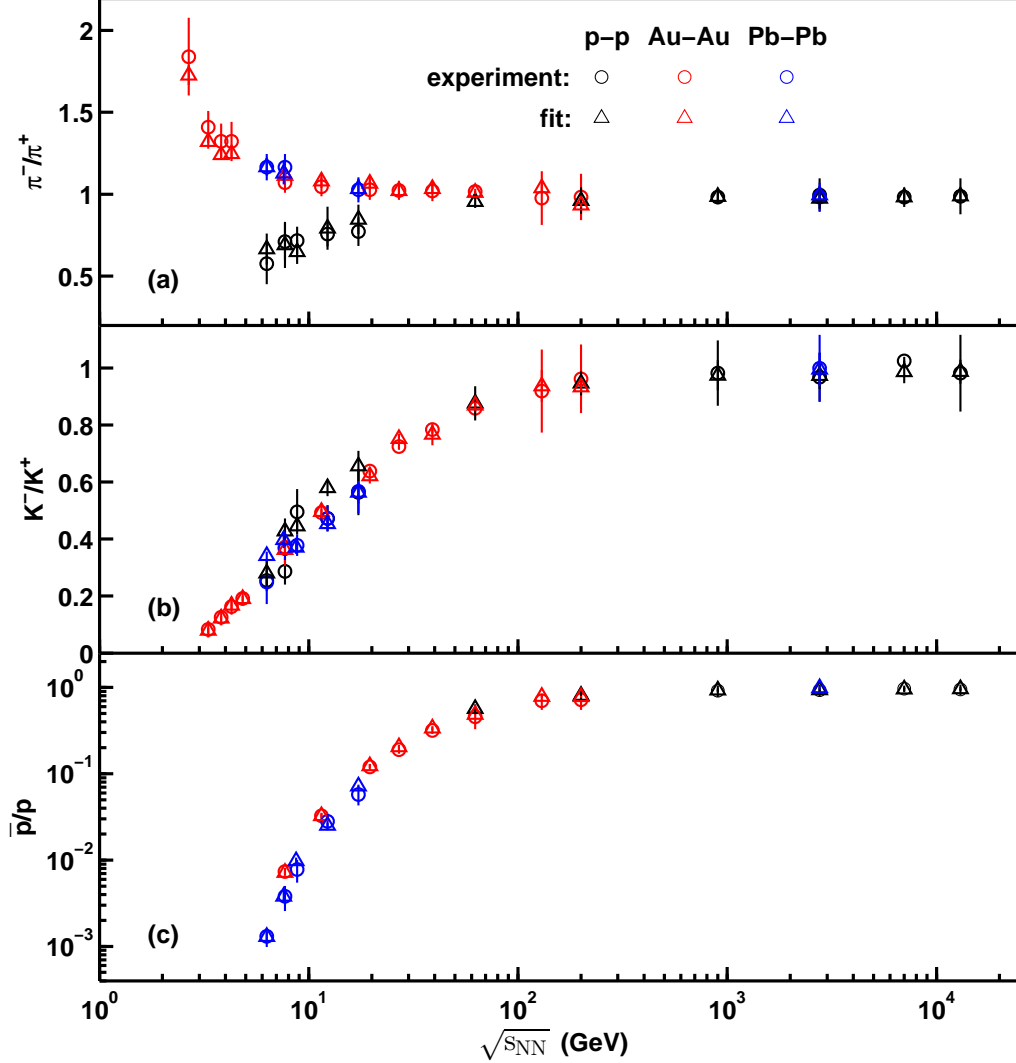


Figure 11. $\sqrt{s_{NN}}$ -dependent yield ratios, π^-/π^+ [Figure 11(a)], K^-/K^+ [Figure 11(a)], and \bar{p}/p [Figure 11(c)]. The black, red, and blue circles denote respectively the calculated results from inelastic pp , central Au-Au, and central Pb-Pb collisions according to normalization constants, and the triangles correspondingly denote the experimental results for comparison.

Based on the corrected yield ratios of negative to positive particles and Equations (8) and (9), the energy dependent chemical potentials, μ_π , μ_K , and μ_p , of light hadrons, π , K , and p , and the chemical potentials, μ_u , μ_d , and μ_s , of light quarks, u , d , and s , are obtained and are shown in Figure 13 with different symbols. The black squares, red circles, and blue triangles denote the calculated results from inelastic pp , central Au-Au, and central Pb-Pb collisions at mid-rapidity, respectively. The curves are the derivative results according to Equations (11)–(14) corresponding to the fitted curves in Figure 12. The

red curves in Figures 13(a), 13(d), 13(e) and 13(f) are the derivative results related to $k_{\pi_{NN}}$ from central nucleus-nucleus collisions, and the black curves are the derivative results related to $k_{\pi_{pp}}$ from inelastic pp collisions or other yield ratios. The solid and dotted curves in Figure 13 correspond to the solid and dotted curves in Figure 13 respectively. In fact, the μ_p in this work is close to the μ_B extracted from thermal fits [34, 71, 72], which indicates to some extent that our calculation of the chemical potential is correct. One can see that, with the increase of $\sqrt{s_{NN}}$ from AGS to LHC, μ_π from central nucleus-nucleus collisions increases obviously and that from inelastic pp collisions decreases obviously, while μ_K , μ_p , μ_u , μ_d , and μ_s from both central nucleus-nucleus and inelastic pp collisions decrease obviously. At the same energy, μ_K is larger than μ_π but less than μ_p , and μ_u is almost as large as μ_d but larger than μ_s due to the difference in mass between different particles. The limiting values of the six types of chemical potentials from central nucleus-nucleus and inelastic pp collisions are zero at very high energy.

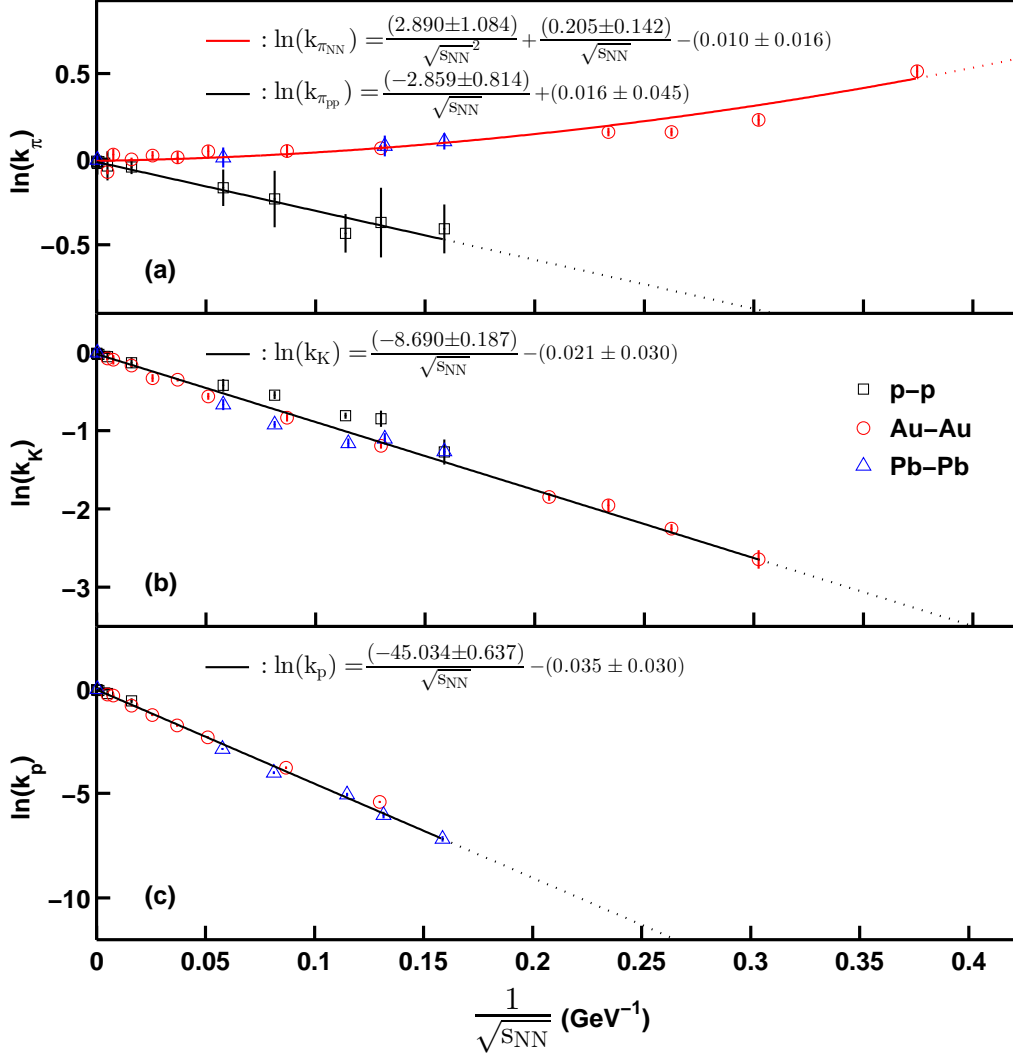


Figure 12. Energy dependent and modified yield ratios. The symbols denote the yield ratios modified by removing strong decay from high-mass resonance and weak decay from heavy flavor hadrons. The curves are the fits according to Equations (11)–(14), respectively.

From Figure 12 one can see that, in central Au-Au and Pb-Pb collisions, $\ln(k_{\pi_{NN}})$ (> 0) increases and $\ln(k_K)$ (< 0) and $\ln(k_p)$ (< 0) decrease obviously with the increase of energy. The difference between

$\ln(k_{\pi_{NN}})$ and $\ln(k_K)$ ($\ln(k_p)$) is caused by different production mechanisms. In the processes of producing pions, kaons, and protons, the difference of cross-section of absorption, content of primary proton in nuclei and so on can result in the difference in the yield of these particles. $\ln(k_{\pi_{NN}}) > 0$ and $\ln(k_{\pi_{pp}}) < 0$ result in $\mu_{\pi_{NN}} > 0$ and $\mu_{\pi_{pp}} < 0$. As the energy increases to the LHC, in both central Au-Au (Pb-Pb) collisions and pp collisions, k_π , k_K , and k_p approach to one, and μ_π , μ_K , and μ_p approach to zero. These same limiting values indicate that hard scattering process possibly plays an important role, mean-free-path of particles becomes largely, and the collision system possibly changes completely from the hadron-dominant state to the quark-dominant state.

In Figure 13, it should be noted that the derived curves of hadron and quark chemical potentials from the fits of the energy dependent yield ratios in Figure 12 simultaneously show a maximum at around 4 GeV, which is not observed from the fits of yield ratios. In order to figure out the accurate energies at these maximums, we make the following calculation according to Equations (6), (8), (9), (11)–(14). For these black curves, whose derivation does not involve Equation (14), we figure out the analytical solutions for the energies at these maximums. The derivation is as follows. From the fits of the logarithms of the three types of yield ratios with $1/\sqrt{s_{NN}}$ in Equations (11)–(13), one can see that all the intercepts on the vertical axes approximate to zero. For simplicity of calculation, we assume that all the intercepts are zero, then Equations (11)–(13) have the following form of

$$\ln(k_i) = \frac{A_i}{\sqrt{s_{NN}}} \quad (i = \pi, K, \text{ and } p), \quad (15)$$

where A_i is the slope. Then, according to Equations (8) and (9), the chemical potential μ_j can be given by

$$\mu_j = T_{ch} \frac{B_j}{\sqrt{s_{NN}}} \quad (j = \pi, K, p, u, d, \text{ and } s), \quad (16)$$

where B_j is a constant. In consideration of T_{ch} given by Equation (6), μ_j can be written as

$$\mu_j = T_{lim} B_j \{ [1 + \exp(2.60 - \ln \sqrt{s_{NN}}/0.45)] \sqrt{s_{NN}} \}^{-1}. \quad (17)$$

Then,

$$\frac{d\mu_j}{d\sqrt{s_{NN}}} = T_{lim} B_j \{ [1 + \exp(2.60 - \ln \sqrt{s_{NN}}/0.45)] \sqrt{s_{NN}} \}^{-2} [1 - (11/9) \exp(2.60 - \ln \sqrt{s_{NN}}/0.45)]. \quad (18)$$

Let $\frac{d\mu_j}{d\sqrt{s_{NN}}} = 0$, then,

$$1 - (11/9) \exp(2.60 - \ln \sqrt{s_{NN}}/0.45) = 0. \quad (19)$$

Finally, we obtain the energy value at the maximum, $\sqrt{s_{NN}} = 3.526$ GeV. One can see that all the energy values at these maximums are the same, which means that in the case of linear fitting (Equations (11)–(13)), the energy is independent of the slope parameter of linear equation. It needs to be emphasized that, in Figure 12, due to the lack of data in low energy region, we can only make prediction about them by the linear fits that can well describe the data points in relatively high energy region. That means the obtained energy value at the maximum is based on the above linear fits. For these red curves, whose derivation involves Equation (14), due to the calculation being complicated, we only give the numerical solutions for the energies at the maximums of these curves. From the data of these derived curves obtained by Equations (6), (8), (9), (11)–(13) in Figure 13, we give the numerical solutions for the energies at the maximums of all curves. From Figure 13(a) to Figure 13(f), the values of the energies at these maximums one by one are 3.584 GeV (for black curve), 3.398 GeV (for red curve), 3.310 GeV, 3.534 GeV, 3.537 GeV (for black curve), 3.590 GeV (for red curve), 3.527 GeV (for black curve), 3.428 GeV (for red curve), 3.521 GeV (for black curve), 3.666 GeV (for red curve). One can see that the energies at these maximum range from 3.310 GeV to 3.666 GeV, and the average value of these energies is 3.510 GeV.

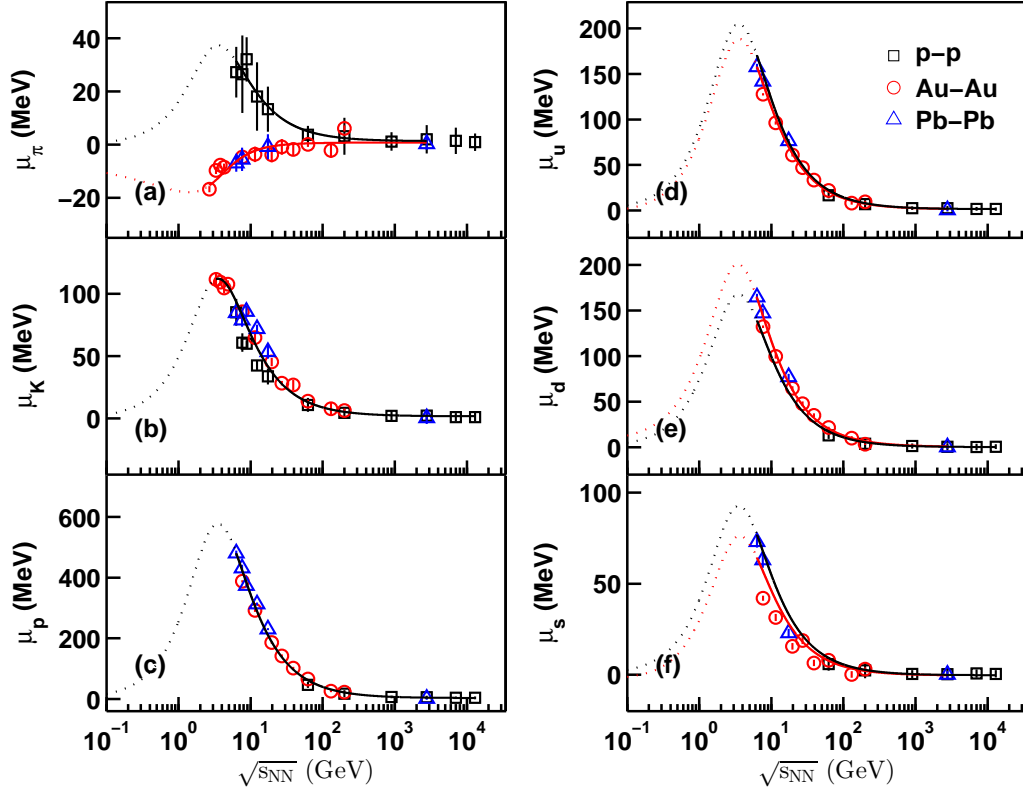


Figure 13. Energy dependent chemical potentials, μ_π [Figure 13(a)], μ_K [Figure 13(b)], and μ_p [Figure 13(c)], of light hadrons, π , K , and p , and μ_u [Figure 13(d)], μ_d [Figure 13(e)], and μ_s [Figure 13(f)], of light quark, u , d , and s . The symbols denote the calculated results according to the modified yield ratios and Equations (8) and (9), and the curves are the derivative results based on the fits of Equations (11)–(14) in Figure 12.

The special energy (around 3.510 GeV) at the maximum possibly is the critical energy of phase transition from a liquid-like hadron state to a gas-like quark state in the collision system, where the liquid-like state and the gas-like state are the states in which the mean-free-path of interacting particles are relatively short and relatively long, respectively. In other words, at this special energy, the collision system starts to change initially its state from the liquid-like nucleons and hadrons to the gas-like quarks, and many properties of the system also change. The curve of proton chemical potential having the maximum at this special energy, indicates that the density of baryon number in nucleus-nucleus collisions has the largest value and the mean-free-path of particles has the smallest value at this special energy, which means that the hadronic interactions play an important role at this stage [73]. When $\sqrt{s_{NN}} > 3.510$ GeV, the chemical potential gradually decrease with increasing $\sqrt{s_{NN}}$, implying that the density of baryon number gradually decreases [73], shear viscosity over entropy density gradually weakens [74], and mean-free-path gradually increases. Meanwhile, the hadronic interactions gradually fade and the partonic

interactions gradually become greater. When $\sqrt{s_{NN}}$ increases to the top RHIC, especially the LHC, all types of chemical potentials approach to zero, when the high energy collision system possibly changes completely from the hadron-dominant state to the quark-dominant state and signifies that the partonic interactions possibly play a dominant role at the top RHIC and LHC [1, 15], and the strongly coupled QGP (sQGP) has been observed [24–26]. It should be pointed out that, due to the lack of experimental data in low energy range, the existence of this maximum is not actually certain. The maximum is only a calculated result according to some empirical formulas, so the energy of critical point is large fluctuations. Although the trend of the chemical potential in low energy region ($\sqrt{s_{NN}} < 3.510$ GeV) is unlikely, the maximum point is at least a turning point, which implies the possibility of phase transition. These results are consistent with our previous work [28]. Our result (around 3.510 GeV) of the critical energy of phase transition is consistent with that (below 19.6 GeV) by the STAR Collaboration [1], and less than the result (between 11.5 GeV and 19.6 GeV) of a study based on the correlation between collision energy and transverse momentum [13–15] and the result (around 62.4 GeV) of the study based on a striking pattern of viscous damping and an excitation function [16]. One can see that although there are many study results, none of them have been confirmed to be reliable. Therefore, we need to continue to study and confirm the exact critical energy of the phase transition.

4 Summary and Conclusion

The transverse momentum (or mass) spectra of final-state light flavour hadrons, π^\pm , K^\pm , p , and \bar{p} , produced in central Au-Au, central Pb-Pb and inelastic pp collisions at mid-rapidity over an energy range from AGS to LHC, are described by a two- or one-component Erlang distribution in the frame of multi-source thermal model. The fitting results are in agreement with the experimental data recorded by the E866, E917, E895, NA49, NA44, NA61/SHINE, PHENIX, STAR, and ALICE Collaborations.

From the fitting parameters, in most cases, the experimental data of p_T (or m_T) spectra are suitable for the two-component Erlang distribution, where the first component corresponding to a narrow low- p_T (or m_T) region is contributed by the soft excitation process in which a few sea quarks and gluons take part in, and the second component corresponding to a wide high- p_T (or m_T) region is contributed by the hard scattering process which is a more violent collision between two valent quarks in incident nucleons. The study shows that the values of the contribution ratio of soft excitation process are more than 50%, which means that the excitation degrees of these collision systems are mainly contributed by the soft excitation processes.

Based on the normalization constants in fitting the transverse momentum or mass spectra of final-state light flavour particles, the final-state yield ratios of negative to positive particles are obtained. The energy dependent chemical potentials of light hadrons, μ_π , μ_K , and μ_p , and quarks, μ_u , μ_d , and μ_s , are extracted from the modified yield ratios in which the contributions of strong decay from high-mass resonance and weak decay from heavy flavor hadrons are removed. With the increase of $\sqrt{s_{NN}}$ over a range from a few GeV to more than 10 TeV, the μ_K , μ_p , μ_u , μ_d , μ_s decrease obviously in central Au-Au, central Pb-Pb, and inelastic pp collisions, while μ_π increases in central Au-Au and Pb-Pb collisions and it decreases in inelastic pp collisions. When collision energy increases to the top RHIC and LHC, all types of chemical potentials are small and the limiting values of them are zero in central Au-Au, central Pb-Pb, and inelastic pp collisions at very high energy.

The logarithms of the yield ratios, $\ln(k_{\pi_{pp}})$, $\ln(k_K)$, and $\ln(k_p)$, show obviously linear dependences on $1/\sqrt{s_{NN}}$ in mentioned energy range, and $\ln k_{\pi_{NN}}$ increases as a polynomial function of $1/\sqrt{s_{NN}}$. Base on the above relationships, we find that at about 3.510 GeV, the derived curves of hadron and quark chemical potentials simultaneously show the maximum. This special energy possibly is the critical energy of phase transition from a liquid-like hadron state to a gas-like quark state in high energy collision system, where the density of baryon number in nucleus-nucleus collisions has a large value and

the hadronic interactions play an important role at this stage. When collision energy increases to the top RHIC, especially the LHC, all types of chemical potentials approach to zero, which indicates that high energy collision system possibly changes completely from the hadron-dominant liquid-like state to the quark-dominant gas-like state and the partonic interactions possibly play a dominant role at the LHC.

Acknowledgments

This work was supported by the National Natural Science Foundation of China under Grant No. 11847114.

Data availability

All data are quoted from the mentioned references. As a phenomenological work, this paper does not report new data.

Conflicts of Interest

The authors declare that there are no conflicts of interest regarding the publication of this paper.

References

- [1] Xu N *et al* (STAR Collaboration) 2014 *Nucl. Phys. A* **931** 1
- [2] Grebieszko K (for the NA61/SHINE Collaboration) 2017 *Acta Phys. Polon. B Proc. Suppl.* **10** 589
- [3] Yang C (for the STAR Collaboration) 2017 *Nucl. Phys. A* **967** 800
- [4] Turko L (for the NA61/SHINE Collaboration) 2018 *Universe* **4** 52
- [5] Braun-Munzinger P and Wambach J 2009 *Rev. Mod. Phys.* **81** 1031
- [6] Wambach J 2007 *Int. J. Mod. Phys. E* **16** 867
- [7] Cleymans J, Oeschler H, Redlich H, and Wheaton S 2006 *Phys. Rev. C* **73** 034905
- [8] Rischke D H 2004 *Prog. Part. Nucl. Phys.* **52** 197
- [9] Cabibbo N and Parisi G 1975 *Phys. Lett. B* **59** 67
- [10] Andronic A, Braun-Munzinger P, and Stachel J 2010 *Nucl. Phys. A* **834** 237c
- [11] Bellwied R 2018 *EPJ Web Conf.* **171** 02006
- [12] Lao H L, Gao Y Q, and Liu F H 2019 *Universe* **5** 152
- [13] Abelev B *et al* (ALICE Collaboration) 2015 *Phys. Rev. C* **91** 024609
- [14] Md.Nasim, Bairathi V, Sharma M K, Mohanty B, and Bhasin A 2015 *Adv. High Energy Phys.* **2015** 197930
- [15] Abelev B I *et al* (STAR Collaboration) 2009 *Phys. Rev. C* **79** 064903
- [16] Lacey R A 2015 *Phys. Rev. Lett.* **114** 142301
- [17] Lacey R A 2014 *Nucl. Phys. A* **931** 904
- [18] Adare A *et al* (PHENIX Collaboration) 2014 [arXiv:1410.2559](https://arxiv.org/abs/1410.2559)
- [19] Borsanyi S, Fodor Z, Hoelbling C, Katz S D, Krieg S, and Szabo K K 2014 *Phys. Lett. B* **730** 99
- [20] Bazavov A *et al* (HotQCD Collaboration) 2014 *Phys. Rev. D* **90** 094503
- [21] Soltz R A, DeTar C, Karsch F, Mukherjee S, and Vranas P 2015 *Ann. Rev. Nucl. Part. Sci.* **65** 379

- [22] Stephanov M A 2006 [arXiv:hep-lat/070100224](https://arxiv.org/abs/hep-lat/070100224)
- [23] Wygas M M, Oldengott I M, Bödeker D, and Schwarz D J 2018 *Phys. Rev. Lett.* **121** 201302
- [24] Bazavov A *et al* 2012 *Phys. Rev. D* **85** 114506
- [25] Adams J *et al* (STAR Collaboration) 2005 *Nucl. Phys. A* **757** 102
- [26] Grosse-Oetringhaus J F (for the ALICE Collaboration) 2014 *Nucl. Phys. A* **931** 22
- [27] Stachel J, Andronic A, Braun-Munzinger P, and Redlich K 2014 *J. Phys.: Conf. Ser.* **509** 012019
- [28] He X W, Wei H R, and Liu F H 2019 *J. Phys. G: Nucl. Part. Phys.* **46** 025102
- [29] Gao Y Q, Lao H L, and Liu F H 2018 *Adv. High Energy Phys.* **2018** 6047960
- [30] Braun-Munzinger P and Stachel J 1998 *Nucl. Phys. A* **638** 3c
- [31] Cleymans J, Kämpfer B, and Wheaton S 2002 *Phys. Rev. C* **65** 027901
- [32] Becattini F, Manninen J, and Gaździcki M 2006 *Phys. Rev. C* **73** 044905
- [33] Andronic A, Braun-Munzinger P, Redlich K, and Stachel J 2007 *Nucl. Phys. A* **789** 334
- [34] Andronic A, Braun-Munzinger P and Stachel J 2006 *Nucl. Phys. A* **772** 167
- [35] Braun-Munzinger P, Stachel J, and Wetterich Ch 2004 *Phys. Lett. B* **596** 61
- [36] Klay J L *et al* (E895 Collaboration) 2003 *Phys. Rev. C* **68** 054905
- [37] Ahle L *et al* (E-802 Collaboration) 1998 *Phys. Rev. C* **58** 3523
- [38] Ahle L *et al* (E866 and E917 Collaborations) 2000 *Phys. Lett. B* **490** 53
- [39] Adamczyk L *et al* (STAR Collaboration) 2017 *Phys. Rev. C* **96** 044904
- [40] Abelev B I *et al* (STAR Collaboration) 2009 *Phys. Rev. C* **79** 034909
- [41] Adcox K *et al* (PHENIX Collaboration) 2004 *Phys. Rev. C* **69** 024904
- [42] Adler S S *et al* (PHENIX Collaboration) 2004 *Phys. Rev. C* **69** 034909
- [43] Alt C *et al* (NA49 Collaboration) 2008 *Phys. Rev. C* **77** 024903
- [44] Alt C *et al* (NA49 Collaboration) 2006 *Phys. Rev. C* **73** 044910
- [45] Afanasiev S V *et al* (NA49 Collaboration) 2002 *Phys. Rev. C* **66** 054902
- [46] Bearden I G *et al* (NA44 Collaboration) 2002 *Phys. Rev. C* **66** 044907
- [47] Abelev B *et al* (ALICE Collaboration) 2013 *Phys. Rev. C* **88** 044910
- [48] Aduszkiewicz A *et al* (NA61/SHINE Collaboration) 2017 *Eur. Phys. J. C* **77** 671
- [49] Adare A *et al* (PHENIX Collaboration) 2011 *Phys. Rev. C* **83** 064903
- [50] Chatrchyan S *et al* (CMS Collaboration) 2012 *Eur. Phys. J. C* **72** 2164
- [51] Sirunyan A M *et al* (CMS Collaboration) 2017 *Phys. Rev. D* **96** 112003
- [52] Liu F H and Li J S 2008 *Phys. Rev. C* **78** 044602
- [53] Liu F H 2008 *Nucl. Phys. A* **810** 159
- [54] Liu F H, Abd Allah N N, and Singh B K 2004 *Phys. Rev. C* **69** 057601
- [55] Liu F H 2008 *Phys. Rev. C* **78** 014902
- [56] Braun-Munzinger P, Magestro D, Redlich K, and Stachel J 2001 *Phys. Lett. B* **518** 41
- [57] Zhao H and Liu F H 2015 *Adv. High Energy Phys.* **2015** 137058
- [58] Andronic A, Braun-Munzinger P, and Stachel J 2009 *Acta Phys. Pol. B* **40** 1005
- [59] Kovács P and Szép Zs 2008 *Phys. Rev. D* **77** 065016
- [60] Arsene I *et al* (BRAHMS Collaboration) 2005 *Nucl. Phys. A* **757** 1
- [61] Klay J L *et al* (E895 Collaboration) 2002 *Phys. Rev. Lett.* **88** 102301

- [62] Akiba Y (E802 Collaboration) 1996 *Nucl. Phys. A* **610** 139
- [63] Adcox K et al (PHENIX Collaboration) 2002 *Phys. Rev. Lett.* **88** 242301
- [64] Abelev B et al (STAR Collaboration) 2010 *Phys. Rev. C* **81** 024911
- [65] Adams J et al (STAR Collaboration) 2004 *Phys. Rev. Lett.* **92** 112301
- [66] Afanasiev S V et al (NA49 Collaboration) 2004 *Phys. Rev. C* **69** 024902
- [67] Abelev B I et al (STAR Collaboration) 2007 *Phys. Rev. C* **75** 064901
- [68] Aamodt K et al (ALICE Collaboration) 2011 *Eur. Phys. J. C* **71** 1655
- [69] Tsallis C 1988 *J. Stat. Phys.* **52** 479
- [70] Yu N and Luo X F 2019 *Eur. Phys. J. A* **55** 26
- [71] Dumitru A, Portugal L, and Zschieche D 2006 *Phys. Rev. C* **73** 024902
- [72] Becattini F, Gaździcki M, Keranen A, and Manninen J *Phys. Rev. C* **69** 024905
- [73] Braun-Munzinger P and Stachel J 2007 *Nature* **448** 302
- [74] Gyulassy M, McLerran L 2005 *Nucl. Phys. A* **750** 30